



저작자표시-비영리-변경금지 2.0 대한민국

이용자는 아래의 조건을 따르는 경우에 한하여 자유롭게

- 이 저작물을 복제, 배포, 전송, 전시, 공연 및 방송할 수 있습니다.

다음과 같은 조건을 따라야 합니다:



저작자표시. 귀하는 원저작자를 표시하여야 합니다.



비영리. 귀하는 이 저작물을 영리 목적으로 이용할 수 없습니다.



변경금지. 귀하는 이 저작물을 개작, 변형 또는 가공할 수 없습니다.

- 귀하는, 이 저작물의 재이용이나 배포의 경우, 이 저작물에 적용된 이용허락조건을 명확하게 나타내어야 합니다.
- 저작권자로부터 별도의 허가를 받으면 이러한 조건들은 적용되지 않습니다.

저작권법에 따른 이용자의 권리는 위의 내용에 의하여 영향을 받지 않습니다.

이것은 [이용허락규약\(Legal Code\)](#)을 이해하기 쉽게 요약한 것입니다.

[Disclaimer](#)

**Effect of plasma electrolytic fluorination and
sacrificial anode design on durability
enhancement of biodegradable magnesium
alloy**

HengBo Jiang

Department of Dentistry

The Graduate School, Yonsei University

**Effect of plasma electrolytic fluorination and
sacrificial anode design on durability
enhancement of biodegradable magnesium
alloy**

Directed by Professor Kwang-Mahn Kim

The Doctoral Dissertation
submitted to the Department of Dentistry,
the Graduate School of Yonsei University
in partial fulfillment of the requirements
for the degree of Ph.D. in Dental Science

HengBo Jiang

June 2017

This certifies that the Doctoral Dissertation
of 'HengBo Jiang' is approved.



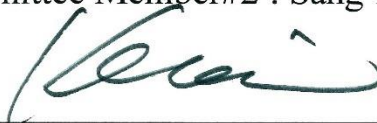
Thesis Supervisor : Kwang-Mahn Kim



Thesis Committee Member#1 : Kyoung-Nam Kim



Thesis Committee Member#2 : Sang-Bae Lee



Thesis Committee Member#3 : Hyung-Jun Kim



Thesis Committee Member#4 : Min-Ho Lee

The Graduate School

Yonsei University

June 2017

ACKNOWLEDGEMENT

My deepest gratitude goes first and foremost to Professor Kwang-Mahn Kim, my supervisor, for his constant encouragement and guidance; he has walked me through all the stages of the writing of this thesis. Without his consistent and illuminating instruction, this thesis could not have reached its present form.

I would like to express my heartfelt gratitude to Professor Kyoung-Nam Kim, Doctor Sang-Bae Lee, Professor Min-Ho Lee, and Professor HyungJun Kim, who taught me how to make my thesis more elegant. I am also greatly indebted to the teachers in my department, who have instructed and helped me a lot over the last three years.

My thanks would go to my beloved mother, father, grandma, and all my relatives and friends for their loving consideration and great confidence in me through the years. I would also like to thank my dear little brother who made a filial request for me to take care of our parents; God will take care of him forever. Finally, I would like to thank my dear fiancée, for her patience, trust, and for encouraging me to complete my Ph.D.

Thanks again to all the people who have helped me.

HengBo Jiang

2017. 06. 14

TABLE OF CONTENTS

LIST OF FIGURES	iii
LIST OF TABLES	vi
ABSTRACT	vii
I. INTRODUCTION	1
1. Magnesium biomaterials	1
2. Surface modification	4
2.1. Fluoride conversion coating	4
2.2. Anodization	5
2.3. Micro-arc fluorination (MAF)	6
3. Corrosion evaluation of Mg	7
3.1. Weight loss test	7
3.2. Hydrogen release test	7
3.3. Potentiodynamic polarization (PDP) test	8
4. Change of mechanical properties through corrosion of Mg	10
5. Research objective and scope	11
II. MATERIALS AND METHODS	12
1. Specimens	12
1.1. AZ31	12
1.2. Plasma electrolytic fluorination (PEF) coating	13
1.3. Indented samples	15
1.4. Corrosion guide design sample	16
2. Simulated body fluid (SBF)	17

3. Surface characterization analysis	18
3.1. FE-SEM and EDS analysis	18
3.2. XRD analysis	18
4. Corrosion test	19
4.1. Potentiodynamic polarization test	19
4.2. Weight loss test	20
5. Tensile test through corrosion	21
6. Pitting corrosion test	22
6.1. Disk type samples analysis	22
6.2. Tensile test samples analysis	22
7. Tensile test of CGD sample through corrosion	23
8. Statistical analysis	24
 III. RESULTS	 25
1. Surface characterization	25
2. Corrosion evaluation	30
3. Tensile test through corrosion	33
4. Pitting corrosion analysis	36
5. Tensile test through the corrosion of CGD samples	41
 IV. DISCUSSION	 44
 V. CONCLUSION	 50
 VI. REFERENCES	 52
 ABSTRACT (in Korean)	 58

LIST OF FIGURES

Figure 1. Schematic diagram of fluoride conversion coating on Mg -----	4
Figure 2. Schematic diagram of Mg anodization -----	5
Figure 3. Schematic diagram of MAF coating on Mg -----	6
Figure 4. Schematic diagram of hydrogen release test on Mg-----	8
Figure 5. Schematic diagram of a one-point bending test (A), three-point bending test (B), and compressive test (C) -----	10
Figure 6. Appearance and size of disc type (A) and tensile test plate (B) samples -----	12
Figure 7. Diagram of PEF coating on AZ31 -----	14
Figure 8. Optical images of indented disc type (A) and tensile test plate (B) sample. Indentations (C) of samples were observed using a microscope-----	15
Figure 9. Planar graph (A) with optical images (B, C) of a CGD sample-----	16
Figure 10. Silicon-sealed tensile test plate (A), silicon-sealed CGD sample (B), after immersion in SBF, removal of silicon, tensile tests were directly performed using an INSTRON testing machine (C) -----	21
Figure 11. The surface morphologies of Bare AZ31 (A), PEF100 (B), PEF110 (C), PEF120 (D), PEF130 (E) and PEF140 (F) (The size of the red bar is 10 μm)-----	25
Figure 12. Cross-sectional images with corresponding EDS maps of PEF100 (A), PEF110 (B), PEF120 (C), PEF130 (D) and PEF140 (E) (The size of the red bar is 10 μm) -----	26

Figure 13. XRD patterns of Bare AZ31 (A), PEF100 (B), PEF110 (C), PEF120 (D), PEF130 (E), and PEF140 (F)-----	27
Figure 14. PDP curves of Bare AZ31 (A), PEF100 (B), PEF110 (C), PEF120 (D), PEF130 (E), and PEF140 (F)-----	28
Figure 15. Percentage weight loss after immersion in SBF for one and four weeks for Bare AZ31 (A), PEF100 (B), PEF110 (C), PEF120 (D), PEF130 (E), and PEF140 (F) (N = 10) ($p = 0.05$)-----	30
Figure 16. Strength–strain curves with its optical images of Bare and PEF- coated AZ31 for: 4 (A), 8 (B), and 12 (C) weeks of corrosion ----	31
Figure 17. Maximum tensile strength after 4, 8, and 12 weeks of corrosion for Bare and PEF-coated AZ31 (N = 10) ($p = 0.05$)-----	32
Figure 18. Potentiodynamic polarization curves of Bare, PEF-coated, indented Bare (in-Bare), and indented PEF-coated (in-PEF) AZ31 -----	33
Figure 19. Optical microscopic images of indented Bare and indented PEF- coated AZ31 before and after immersion in SBF for one week ---	34
Figure 20. Optical images of Bare, PEF-coated, indented Bare (in-Bare), and indented PEF-coated (in-PEF) AZ31 before and after immersion in SBF for two weeks -----	35
Figure 21. Strength–strain curves (A) and mean maximum strength (B) after two weeks of corrosion for Bare, PEF-coated, indented Bare (in- Bare), and indented PEF-coated (in-PEF) AZ31 (N = 10) ($p = 0.05$) -----	36
Figure 22. Strength–strain curves with optical images for Bare and PEF- coated AZ31 and a CGD sample after 4 (A), 8 (B), and 12 (C) weeks of corrosion (N = 10) ($p = 0.05$) -----	37

Figure 23. The mean maximum tensile strength for each specified period of corrosion for Bare and PEF-coated AZ31 and the CGD sample ($N = 10$) ($p = 0.05$) -----38

LIST OF TABLES

Table 1. Summary of the physical and mechanical properties of various implant materials compared to natural bone (Staiger et al., 2006) ----	3
Table 2. Elements and concentrations in AZ31 (wt%)-----	12
Table 3. Sample codes with PEF treatment conditions -----	14
Table 4. Components with content in SBF (mg/L) -----	17
Table 5. Results of the potentiodynamic polarization test for Bare and PEF- coated AZ31. The corrosion potential (E_{corr}), current density (i_{corr}) and corrosion rate (CR) were measured using software (VersaStudio 2.44.4)-----	29

ABSTRACT

Effect of plasma electrolytic fluorination and sacrificial anode design on durability enhancement of biodegradable magnesium alloy

HengBo Jiang

Department of Dentistry

The Graduate School, Yonsei University

(Directed by Professor Kwang-Mahn Kim, D.D.S., Ph.D.)

Magnesium (Mg) and its alloys have attracted fundamental research in the fields of orthopedics, cardiovascular, and dentistry as biodegradable metallic materials. However, Mg exhibits poor corrosion resistance, especially in a physiological environment, which limits its applicability in medical applications.

This study uses a type of Mg alloy called AZ31. The corrosion resistance of AZ31 was improved using plasma electrolytic

fluorination (PEF) as a surface treatment. Then, the surface morphology, coating thickness, and composition were observed, and the corrosion behaviors of PEF-coated AZ31 were evaluated via electrochemical and weight loss tests. The tensile strength of PEF-coated AZ31 after immersion in simulated body fluid (SBF) was investigated after 4, 8, and 12 weeks and compared with Bare AZ31 which underwent the same treatment. Pitting corrosion caused a rapid decline in the mechanical strength of AZ31. We verified pitting corrosion using the hardness tester to indent the surface of the samples and performed pitting corrosion analysis. In addition, we prevented the rapid corrosion of AZ31 by designing a “corrosion guide design (CGD)” for the unprecedented Mg implant according to the potential difference between Bare and PEF.

The result of coating with PEF showed that a porosity structure of pore size 600–900 nm and thickness 1–14 μm was generated on the AZ31 substrate. MgF_2 was covered on the coated surface. In electrochemical corrosion and immersion corrosion tests, the PEF-coated AZ31 exhibited efficiently improved corrosion resistance compared to Bare AZ31 in SBF. In the results of tensile strength through corrosion, the growth trend of weight loss percentage for PEF-coated AZ31 was less than that of Bare AZ31. However, the tensile strength of the PEF-coated AZ31 after immersion was lower than that of Bare AZ31. We verified that the pitting corrosion was the main reason why the strength of PEF-coated AZ31 was lost rapidly. As seen in the results, the CGD can fully protect the strength of the AZ31, but only for a period time.

Although the PEF coating has a structure that favors biological growth and it can increase the corrosion resistance of AZ31, there is a limitation in its clinical use because of its generation of pitting corrosion. The result in the PEF-coated AZ31 could lead to mechanical fracture through biodegradation. However, after surface-treatment, Mg could have increased corrosion resistance but the pitting corrosion might rapidly reduce the mechanical strength of an Mg implant, resulting in serious consequences for patients. Perhaps the CGD would remedy the disadvantages of surface coating technology on applying biomedical Mg implants.

Key words; Magnesium implant, Plasma electrolytic fluorination, Tensile test, Corrosion resistance, Biodegradable materials, Pitting corrosion, Corrosion guide design

Effect of plasma electrolytic fluorination and sacrificial anode design on durability enhancement of biodegradable magnesium alloy

HengBo Jiang

*Department of Dentistry
The Graduate School, Yonsei University*

(Directed by Professor Kwang-Mahn Kim, D.D.S., Ph.D.)

I. INTRODUCTION

1. Magnesium biomaterials

In recent years, Mg and its alloys have often been studied as biodegradable materials for medical applications (Wang et al., 2012).

Common implant materials such as stainless steel, cobalt chrome and titanium alloys have densities in the range 3.1–9.2 g/cm³, whereas the density of natural bone is 1.8–2.1 g/cm³. Mg alloys are more comparable at a density of 1.74–2.0 g/cm³ (Staiger et al., 2006; Witte et al., 2008), and Mg alloys are also much more comparable to natural bone than other

materials with regard to fracture toughness, elastic modulus, and compressive yield strength (Song and Song, 2007), which are shown in Table 1.

Table 1. A summary of the physical and mechanical properties of various implant materials compared to natural bone (Staiger et al., 2006)

Properties	Natural bone	Mg alloy	Ti alloy	Co–Cr alloy	Stainless steel	Synthetic HA
Density (g/cm ³)	1.8–2.1	1.74–2.0	4.4–4.5	8.3–9.2	7.9–8.1	3.1
Elastic modulus (GPa)	3–20	41–45	110–117	230	189–205	73–117
Compressive yield strength (MPa)	130–180	65–100	758–1117	450–1000	170–310	600
Fracture toughness (Mpa ^{1/2})	3–6	15–40	55–115	N/A	50–200	0.7

Mg is nontoxic and the fourth most essential element in the human body; redundant Mg cations can be harmlessly excreted in urine (Staiger et al., 2006). In addition, Mg implants can biodegrade through corrosion, which eliminates the need for a second surgery to remove them (Shi et al., 2009).

However, from a practical perspective, pure Mg is incapable of providing the mechanical properties that are required in many implant applications (Vojtěch et al., 2006; Ganeshan et al., 2009). The modern portfolio of commercial Mg alloys has evolved to include compositions that contain aluminum (Al) (Kannan et al., 2008), zinc (Zn) (Zhang et al., 2010), calcium (Ca) (Kirkland et al., 2010), lithium (Li) (Li et al., 2006),

manganese (Mn) (Xu et al., 2007), and rare earth elements (RE) (Hort et al., 2010). Such alloys have been developed on the basis of their physical properties such as strength and ductility. Thus, the vast majority of studies to date have been performed on commercial alloys. The most common Mg alloys in the field of biodegradable research are AZ series Mg alloys such as AZ31 (Willbold et al., 2011; Iglesias et al., 2015) and AZ91 (Wang et al., 2009; Razavi et al., 2015).

However, the degradation rate of bare Mg alloy in human body fluids is rather high, and when using Mg alloy as an implant it cannot maintain sufficient mechanical integrity during the tissue union period (Zeng et al., 2006). In addition, the Mg alloy in the body has a rapid corrosion reaction that produces a large amount of gas bubbles. Thus, bone tissue healing could be disturbed by the gaseous reaction (Witte, 2015).

2. Surface modification

Mg implants have limited use in clinical applications because Mg in the body undergoes rapid corrosion. Thus, the key issue in the development of degradable Mg implants is reducing the corrosion rate. Currently, several methods of surface modification of Mg have been studied such as anodization (Jiang et al., 2014; Mousa et al., 2016; Zhang et al., 2016b), polymer coatings (Ostrowski et al., 2013; Wan et al., 2014; Xu and Yamamoto, 2012), ceramic coatings (Lin et al., 2016; Zhang et al., 2016a), and fluoride conversion coating (Chiu et al., 2007; Sun et al., 2016; Thomann et al., 2010) for improving the corrosion resistance.

2.1. Fluoride conversion coating

One method of fluoride conversion coating is of particular interest for Mg implants, because it can create a fluoride coating that is effective at improving corrosion resistance, and uses a very simple process (Chiu et al., 2007). However, this method requires a processing time of at least 24 hours, and controlling the specified coating thickness is difficult (Chiu et al., 2007; Sun et al., 2016). The schematic diagram of fluoride conversion coating on Mg is as shown in Figure 1.

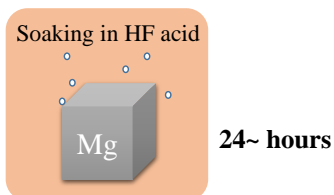
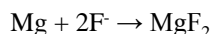


Figure 1. Schematic diagram of fluoride conversion coating on Mg.

2.2. Anodization

Anodization is one of the most commonly used surface treatment technologies that can efficiently control the coating structure and thickness by changing the voltage and current over a short processing time (Jiang et al., 2014; Peixoto Barbosa and Knörschild, 2009; Song and Shi, 2014). In anodization, a layer of oxides is formed via electrolysis on the surface of the metal that enhances the metal's corrosion resistance (Cai et al., 2011). Figure 2 shows a schematic diagram of a common setup for the anodization of Mg. Most anodized Mg is generated as an oxide (MgO) layer. Although MgO is useful for improving the corrosion resistance (Han et al., 2013), this form of anodized Mg is still incapable of creating the desired effect because of the appearance of cracks (Ezhilselvi et al., 2016; Němcová et al., 2013; Wilke et al., 2016).

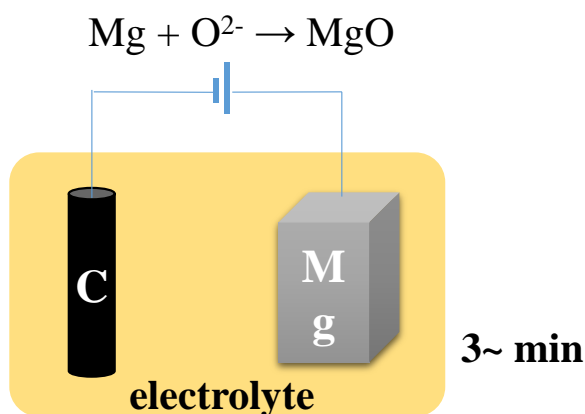


Figure 2. Schematic diagram of Mg anodization.

2.3. Micro-arc fluorination (MAF)

MAF technology was introduced in 2014 (Jiang et al., 2014). This can be combined with the advantages of fluoride coating and anodization on Mg to increase the corrosion resistance. The MAF coating was fabricated in a saturated NH_4HF_2 solution at 120–200 V through a DC power supply (Figure 3); the coating has a porous structure and was mainly composed of MgF_2 . MAF-coated Mg has high corrosion resistance and good biocompatibility. Furthermore, compared to a smooth surface, a rough surface allows cells to stick more easily and start growing (Kunzler et al., 2007).

In addition, compared to the processing time for soaking Mg in HF solution (Chiu et al., 2007; Witte et al., 2010; Yan et al., 2010), MAF treatment greatly reduces the processing time, which is highly convenient for research and development.

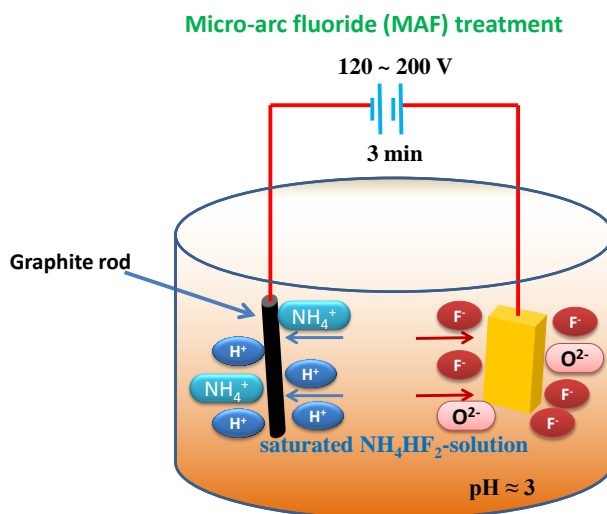


Figure 3. Schematic diagram of MAF coating on Mg.

3. Corrosion evaluation of Mg

There are several commonly used tests, from simple immersion or weight loss (mass loss) experiments to electrochemical investigations that provide mechanistic information about how material degrades.

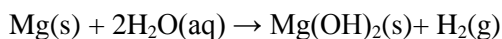
3.1. Weight loss test

Weight loss measurement is perhaps the simplest *in vitro* method available for investigating Mg corrosion (Vojtech et al., 2006; Wang and Shi, 2011). Setup may vary depending on the experimental variables such as the choice of buffering system, but the same design is typically employed that requires only a sample, solution, and an accurate microbalance.

During the test, the sample is placed in a selected solution for a set period of time, after which it is removed and its weight loss is measured. Normally, a mixture such as dilute chromic acid is used to remove any corrosion products on the surface (Chiu et al., 2007; Hort et al., 2010).

3.2. Hydrogen release test

The corrosion reaction for Mg in electrolyte environment is:



This indicates that one atom of Mg will generate one H₂ gas molecule; in other words, the evolution of one mol of H₂ gas directly corresponds to the dissolution of one mol of Mg. Consequently, measuring the volume of H₂ gas produced is theoretically equivalent to measuring the Mg weight loss.

The basic set-up of a H_2 evolution experiment is similar to that of a standard weight loss experiment. Typically, a sample is immersed in an SBF. For most setups, this involves the use of an inverted funnel and burette or graduated tube (Eliezer and Witte, 2010; Liu et al., 2010; Müller et al., 2007; Takadama et al., 2004). Prior to the investigation, the burette is filled with a test solution, and the H_2 gas will rise and replace the solution in the burette as it evolves. The schematic diagram of hydrogen release test for Mg is as shown in Figure 4.

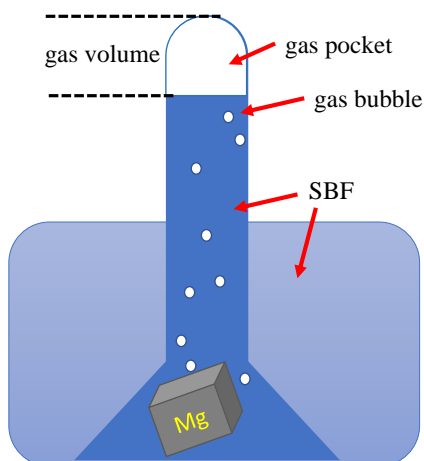


Figure 4. Schematic diagram of hydrogen release test on Mg.

3.3. Potentiodynamic polarization (PDP) test

Potentiodynamic polarization is currently the most commonly used electrochemical technique for studying the corrosion of Mg alloys (Biribilis et al., 2009; Flitt and Schweinsberg, 2005). Typically, tests start with a set period of time in which the open circuit potential (OCP) is recorded (AST M Standard G102-89). This allows the material surface to stabilize with the electrolyte and reach a near-steady potential. Following this, an applied

potential is imposed between the working and counter electrode. The potential is altered at a controlled rate, and the current required for this change to occur is recorded. Normally for Mg, the potential is initially set to be more negative and sweeps up to become more positive than the OCP. This limits the effect of the increased Mg dissolution that occurs in the anodic region (Wang, 2006).

4. Change in mechanical properties through corrosion of Mg

Mechanical performance is the most important consideration for biodegradable Mg alloys, because fast degradation may induce early mechanical loss before the tissue has had time to heal (Wang et al., 2011; Witte, 2015).

There are a few previous reports on the mechanical properties of Mg alloys through corrosion either *in vitro* or *in vivo*. These include a one-point bending test (Figure 5A) (Tan et al., 2014), a three-point bending test (Figure 5B) (Yan et al., 2010), and a compressive test (Figure 5C) (Dezfuli et al., 2017).

However, experiments on the tensile strength of Mg alloys after corrosion have not yet been conducted. It is generally believed that tensile tests are most required to reflect the mechanical properties of metallic material.

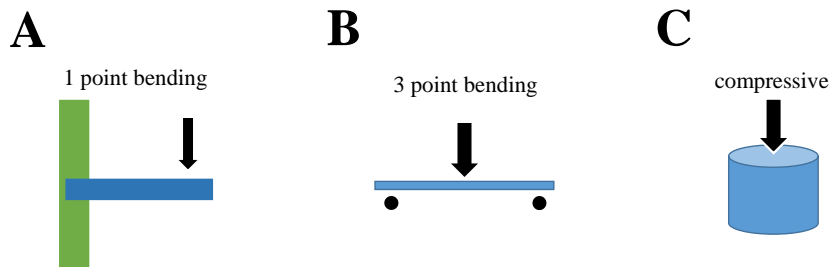


Figure 5. Schematic diagram of a one-point bending test (A), three-point bending test (B), and compressive test (C).

5. Research objective and scope

This study carries out tests on AZ31 Mg alloy. In addition, we have developed a new fluoride coating technology called “plasma electrolytic fluorination” (PEF) that creates a fluoride coating on the AZ31 and reduces the required processing time. Its innovation is in the electrolyte, and its fluorine concentration is much higher than a traditional hydro fluoride acid and MAF electrolyte.

Then, the surface microstructure, composition, crystal structure, corrosion rate, and tensile strength through the corrosion of PEF-coated AZ31 were measured and evaluated.

The aim of this study is to increase the corrosion resistance of AZ31 with PEF. Therefore, the hypothesis is that corrosion rate of PEF-coated AZ31 is lower than for Bare AZ31. Hence, the tensile strength of PEF-coated AZ31 is higher than Bare AZ31 through corrosion.

The possibility of rapid corrosion on PEF-coated AZ31 is prevented by also preparing a new type of Mg-implant design called the CGD for increasing the strength durability. The principle of this design is similar to the “sacrificial anode” or “cathodic protection” that exposes the Mg substrate at the end of the PEF-coated Mg. Thus, we hold that the strength of the CGD sample remains unchanged within a certain time range.

II. MATERIALS AND METHODS

1. Specimens

1.1. AZ31

A commercial AZ31 sheet (Dongguan FeiTai Metal Products Co., Ltd., China) was laser-cut into types of disc and tensile test plates; these sizes were as shown in Figure 6. The ingredients of the alloy are listed in Table 2. All samples were polished progressively with SiC paper from grade #600 up to grade #2000 in absolute ethyl alcohol. The samples were then ultrasonically washed in absolute ethyl alcohol for one minute and blow dried.

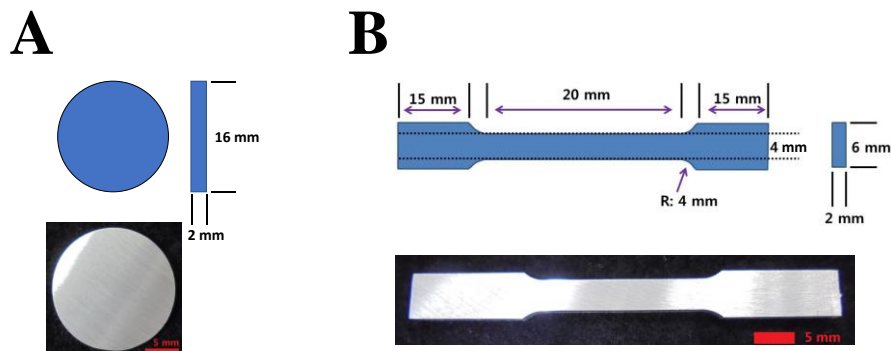


Figure 6. Appearance and size of disc type (A) and tensile test plate (B) samples.

Table 2. Elements and concentrations in AZ31 (wt. %)

Element	Al	Zn	Mn	Fe	Cu	Ni	Si	Mg
Concentration	2.85	0.75	0.62	0.0029	0.00045	0.00052	0.025	rest

1.2. Plasma electrolytic fluorination (PEF) coating

This fluoride treatment process was designated PEF, according to plasma electrolytic oxidation (PEO) technology. Figure 7 shows a diagram of the PEF coating process.

The ultra-high concentration of fluorine electrolyte should be prepared by heating pure NH_4HF_2 (DAEJUNG CHEMICALS & METALS CO., LTD, Korea) to its molten state. The heater temperature (150°C) should then be controlled to maintain the melting status in an electrolytic cell because the electrolyte was at a high temperature and contains a high concentration of fluoride. Therefore, the electrolytic cell must be made of high temperature-resistant plastic.

PEF equipment uses a DC constant voltage power supply. Bare AZ31 was used as the anodic electrode, and a graphite rod was used as the cathodic electrode. The electrodes were soaked in the fluorine electrolyte, and treatment voltages of 100–140 V were applied for 30 seconds; the sample name code with the conditions of surface treatment is provided in Table 3. During the PEF process, the electrolyte was stirred with a polytetrafluoroethylene (PTFE)-coated magnetic bar. After treatment, the samples were rinsed in distilled water and blow-dried.

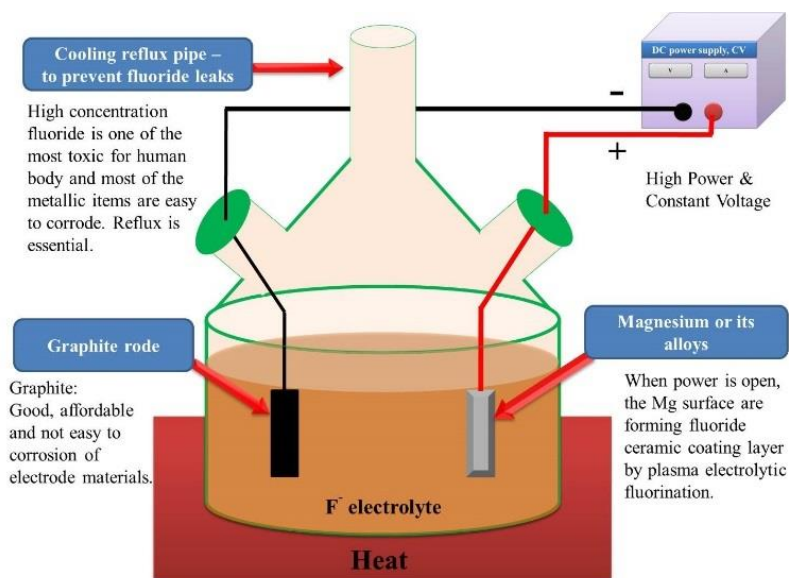


Figure 7. Diagram of PEF coating on AZ31.

Table 3. Sample codes with PEF treatment conditions

Sample code	Operation	Electrolyte	DC power supply (V)	Treatment time (s)
Bare	untreated	-	-	-
PEF ₁₀₀	Anodized	Molten NH ₄ HF ₂	100	30
PEF ₁₁₀	Anodized	Molten NH ₄ HF ₂	110	30
PEF ₁₂₀	Anodized	Molten NH ₄ HF ₂	120	30
PEF ₁₃₀	Anodized	Molten NH ₄ HF ₂	130	30
PEF ₁₄₀	Anodized	Molten NH ₄ HF ₂	140	30

1.3. Indented samples

The samples used were a type of disc and tensile test plate, and four test groups: Bare, PEF, indented Bare, and indented PEF were observed. The indentation was pressed to 0.5 mm depth by a Vickers hardness tester (Matsuzawa DMH-2, Japan), as seen in Figure 8.

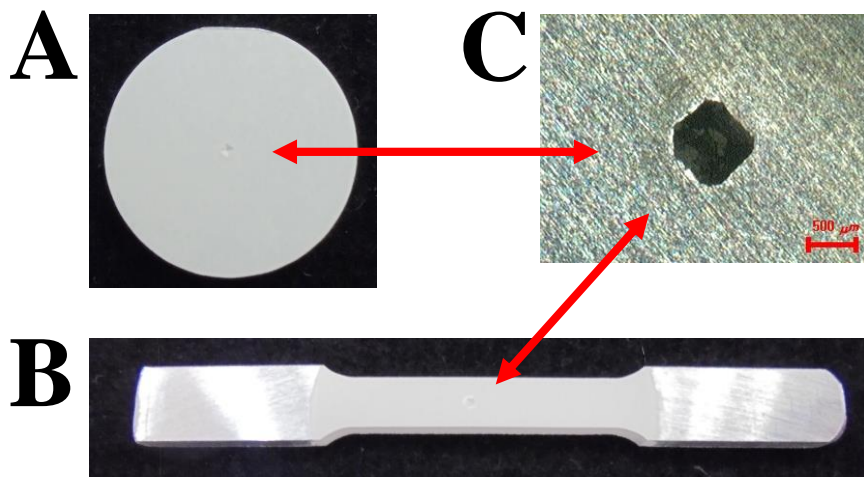


Figure 8. Optical images of indented disc type (A) and tensile test plate (B) samples. Indentation (C) of samples was observed using a microscope.

1.4. Corrosion guide design sample

The corrosion guide was designed according to the different potential in the matrix and PEF coatings of AZ31. The CGD sample was produced as shown in Figure 9; the surface of its leakage was for the sake of purposeful corrosion to protect the specified area of the PEF-coated AZ31.

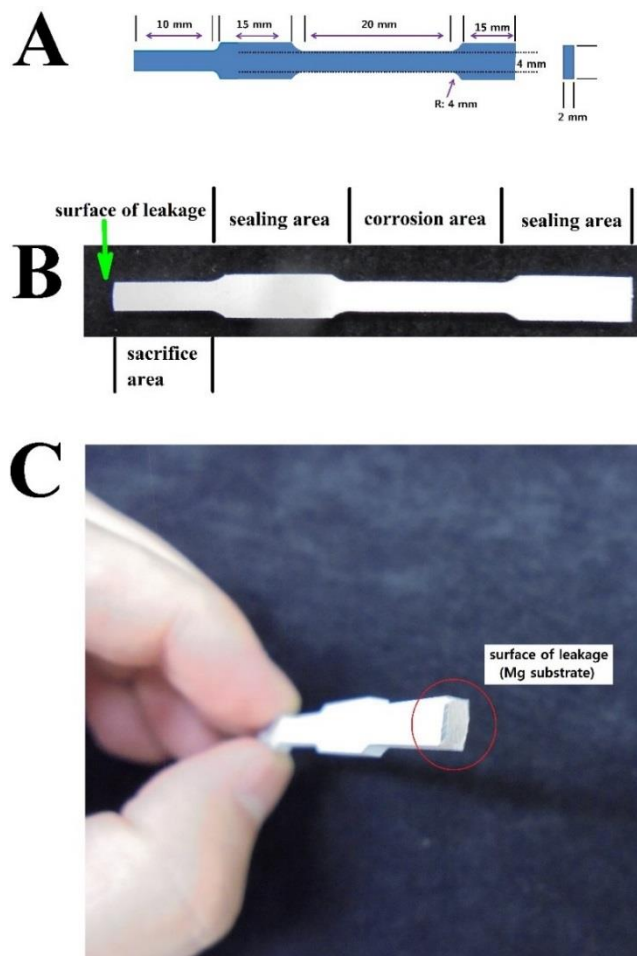


Figure 9. Planar graph (A) with optical images (B, C) of a CGD sample.

2. Simulated body fluid (SBF)

The corrosion measurement experiments used a commercial Hank's balanced salt solution (HBSS, WELGENE Inc. Korea) as the SBF for all corrosion tests. The components and concentration of SBF were as provided in Table 4.

Table 4. Components with content in SBF (mg/L)

Component	CaCl ₂	MgSO ₄	KCl	KH ₂ PO ₄	NaHCO ₃	NaCl	Na ₂ HPO ₄	D-Glucose
Content	140	98	400	60	350	8000	48	1000

3. Surface characterization analysis

3.1. FE-SEM and EDS analysis

The surface morphology of the samples was observed via field emission scanning electron microscopy (FE-SEM, ZEISS Supra 40VP), and the distribution of elements was determined via energy dispersive spectrometry (EDS).

3.2. XRD analysis

The surface crystal structure of the samples was determined via X-ray diffraction (XRD, Rigaku Ultima IV, Japan) with the Cu-K $_{\alpha}$ line at 40 kV and 30 mA, with 2θ in the range 20–80° with a 1°/min scan rate.

4. Corrosion test

The disk type samples were used in the corrosion test.

4.1. Potentiodynamic polarization (PDP) test

Electrochemical tests were performed and analyzed with a potentiostat (VersaSTAT 3:300) and commercial software (VersaStudio 2.44.4). The electrochemical cell consisted of a classical three-electrode cell that included a working electrode to be used as the test sample. Pure graphite was used as the counter electrode, and Ag/AgCl/Sat-KCl (+197 mV vs. a standard hydrogen electrode) was the reference electrode. The samples were positioned in a sealed PTFE clamp with an exposed surface area of 0.9 cm^2 as the working electrode. SBF (1000 ml) in electrolyte form was contained in a double-wall beaker, and the temperature of the electrolyte was maintained at 37°C using a circulating water heater.

In this experiment, the samples were immersed in the SBF for one hour to execute their open circuit potential (OCP) mode and thus ensure that the test samples' potential remained stable. After the OCP, PDP was executed. The samples were scanned from the cathodic region to the anodic region at a rate of 5 mV/s. The corrosion potential (E_{corr}), current density (i_{corr}), and corrosion rate (CR) were measured using software.

4.2. Weight loss test

In the weight loss test, the samples were vertically immersed in SBF and maintained at 37°C for one and four weeks. The ratio of the SBF volume to the sample area was 20 ml/cm² as per ASTM standard G31-74, and the SBF was replaced every week. After one and four weeks, samples were ultrasonically washed in 20% chromium trioxide solution for one minute. The samples were then rinsed with absolute ethanol and dried; the percentage of weight loss was calculated as follows:

$$\text{Weight loss \%} = \frac{W_0 - W_1}{W_0} \times 100 \%$$

Where:

w_0 = the weight of the samples before the test,

w_1 = the weight of the samples after the test.

Ten samples of each group were tested, and the percentage weight loss was expressed as the mean \pm standard deviation (SD).

5. Tensile test through corrosion

The tensile strength was checked through immersion in SBF; we set the mark of the “corrosion area” and “sealing area” on the tensile test samples. We ensured that the grips of the sample did not participate in the degradation and only allowed the corrosion area to degrade by sealing the bilateral grips with silicon; the mean length of the corrosion area was 30 mm (Figure 10A, B). Then, the sealed samples were immersed in SBF and maintained at 37°C for 4, 8, and 12 weeks. The ratio of the SBF volume to the corrosion area was 20 ml/cm² and the SBF was replaced every week. After each four-week period, ten samples from the Bare and PEF groups were removed from the silicon, and tensile testing was performed using an INSTRON testing machine at a constant cross-head speed of 1 mm/min (Figure 10C); the tensile curves were recorded.

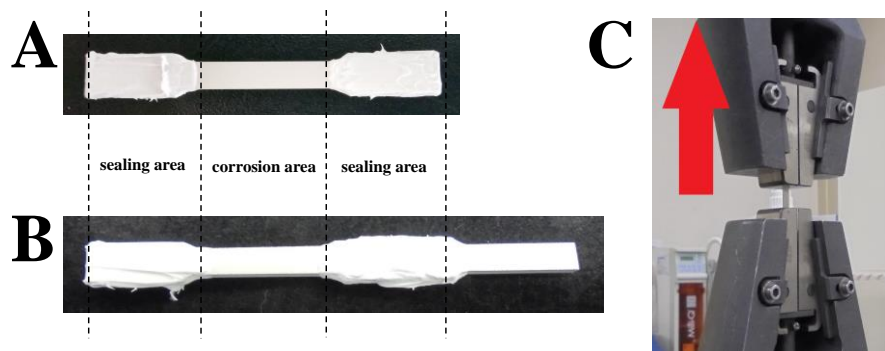


Figure 10. Silicon-sealed tensile test plate (A), silicon-sealed CGD sample (B), after immersion in SBF and removal of the silicon, tensile tests were directly performed using an INSTRON testing machine (C).

6. Pitting corrosion analysis

We verified that the pitting corrosion was the main reason why the strength of the PEF-coated AZ31 reduced rapidly by considering indentation on the surface of Bare and PEF-coated samples (See Figure 8).

6.1. Disk type sample analysis

The PDP test and immersion test were conducted using disk type samples. The PDP test was consistent with the materials and method described in Section 4.1. In the immersion test, indented Bare and indented PEF-coated AZ31 were vertically immersed in SBF and maintained at 37°C for one week. The ratio of the SBF volume to the sample area was 20 ml/cm². After one week of immersion, the samples were taken out and blow dried. The surface of the indented sample was then observed with a microscope.

6.2. Tensile test samples analysis

This method was consistent with the materials and method described in Section 5. Four testing groups of Bare, PEF, indented Bare, and indented PEF samples were vertically immersed in SBF and maintained at 37°C for two weeks; the ratio of the SBF volume to the sample area was 20 ml/cm². After two weeks of corrosion, ten samples from each group were removed from their silicon and tensile testing was performed with an INSTRON testing machine at a constant cross-head speed of 1 mm/min (Figure 10C); the tensile curves were recorded.

7. Tensile test of CGD sample through corrosion

This method was consistent with the materials and method in Section 5. The bilateral grips were sealed with silicon to ensure that the grips of the CGD sample did not participate in the degradation, and only the corrosion area was allowed to degrade (Figure 10B). Then, the sealed samples were immersed in SBF and maintained at 37°C for 4, 8, and 12 weeks. The ratio of the SBF volume to the corrosion area was 20 ml/cm² and the SBF was replaced every week. After every four-week period, ten samples of Bare, PEF, and CGD groups had the silicon removed and underwent tensile testing using an INSTRON testing machine at a constant cross-head speed of 1 mm/min (Figure 10C), and tensile curves were recorded.

8. Statistical analysis

Ten samples of each group were tested, and the value of the percentage of weight loss and tensile strength were expressed as mean \pm standard deviation (SD).

Statistical analysis of the results was carried out using one-way analysis of variance (ANOVA) with *post hoc* analysis of Tukey's test. Values for which $p = 0.05$ were considered significant.

III. RESULTS

1. Surface characterization

The surface morphologies of Bare and PEF-coated AZ31 were as shown in Figure 11. Several different structural coatings formed on the surfaces of the PEF-coated AZ31. For the coatings that were formed at less than 120 V by PEF, the initial analysis of the surfaces disclosed a rough structure with a nonuniform texture (Figure 11B, C). Once an anodizing voltage above 120 V was applied, the surfaces of the PEF coatings formed a relatively fine porous and uniform structure. The diameters of the pore size for PEF₁₂₀, PEF₁₃₀, and PEF₁₄₀ were approximately 600, 700, and 900 nm, respectively, as shown in Figure 11D-F.

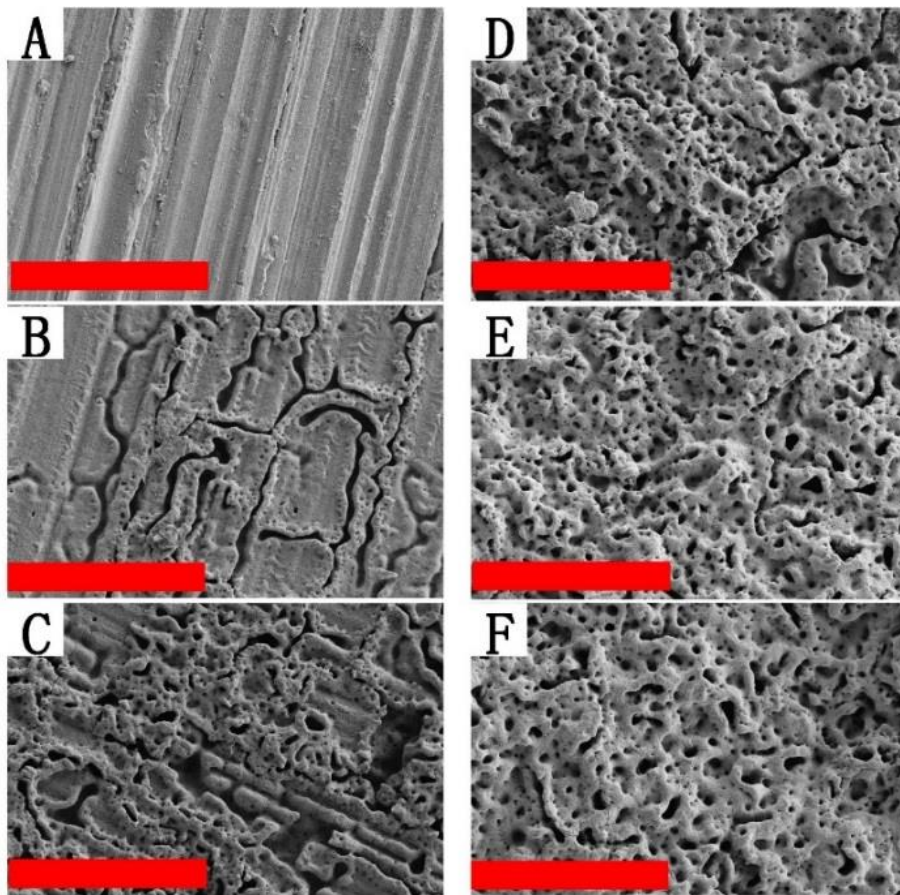


Figure 11. The surface morphologies of Bare AZ31 (A), PEF₁₀₀ (B), PEF₁₁₀ (C), PEF₁₂₀ (D), PEF₁₃₀ (E), and PEF₁₄₀ (F). (The size of the red bar is 10 μm).

Figure 12 displays the cross-sectional morphology and corresponding distribution of fluoride and magnesium elements by EDS maps of the PEF-coated AZ31. The distribution of the elements is indicated by the red (fluoride) and green (magnesium) color. In accordance with the distribution of fluoride and magnesium, we could observe that the fluoride layers were uniformly distributed on the Mg substrates. The thickness of the fluoride coating layers of PEF₁₀₀, PEF₁₁₀, PEF₁₂₀, PEF₁₃₀, and PEF₁₄₀ were 1.3 μm , 2.7 μm , 5.6 μm , 13.6 μm , and 13.9 μm , respectively.

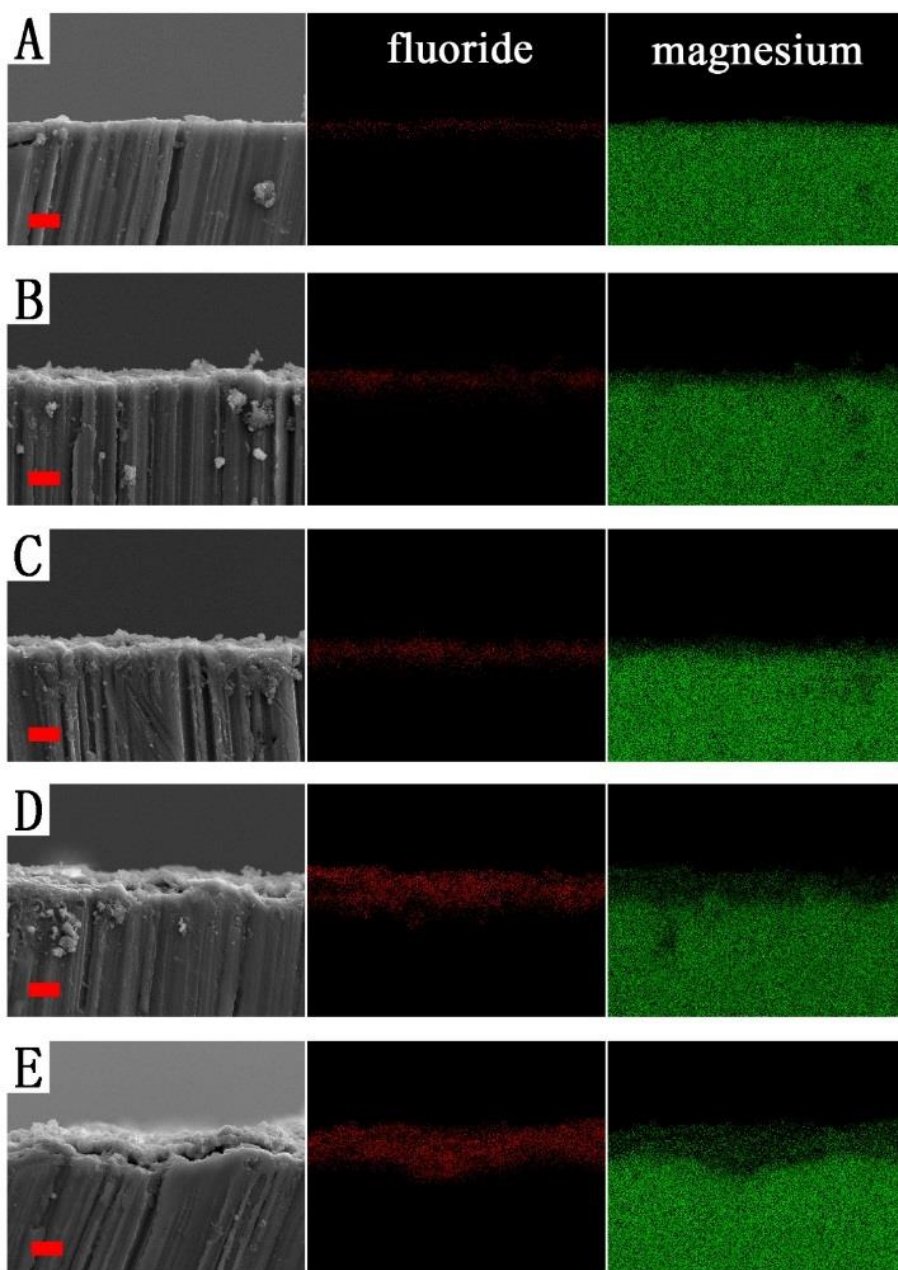


Figure 12. Cross-sectional images with corresponding EDS maps of PEF₁₀₀ (A), PEF₁₁₀ (B), PEF₁₂₀ (C), PEF₁₃₀ (D), and PEF₁₄₀ (E). (The size of the red bar is 10 μm).

Figure 13 shows normalized XRD curves for Bare and PEF AZ31. The comparison of the Bare AZ31 with the standard JCPDS card shows that the PEF coating was mainly composed of tetragonal MgF_2 (JCPDS No. 41-1443). The peak height of the MgF_2 was higher for an increased anodizing voltage.

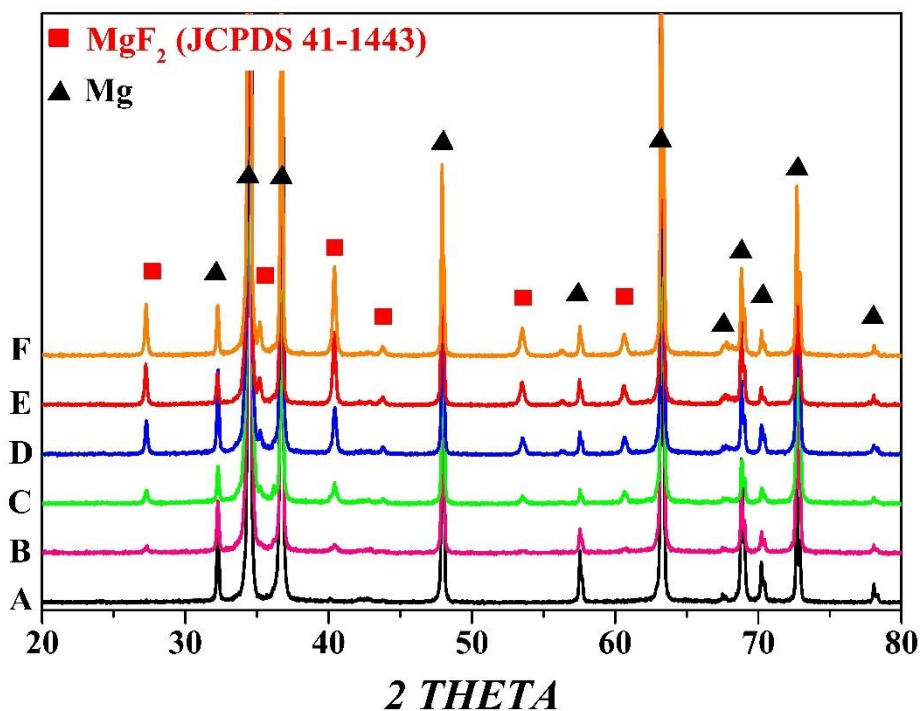


Figure 13. XRD patterns of Bare AZ31 (A), PEF_{100} (B), PEF_{110} (C), PEF_{120} (D), PEF_{130} (E), and PEF_{140} (F).

2. Corrosion evaluation

Figure 14 shows the potentiodynamic polarization curves of Bare and PEF AZ31. According to the result, we can infer that the increase in the treatment voltages of the anodization accompanies a shift to lower current density values in the polarization curve of the samples, confirming that the corrosion resistance of the PEF-coated AZ31 was enhanced. The values for the corrosion potential (E_{corr}), current density (i_{corr}), and the corrosion rate (CR) obtained from Figure 14 are listed in Table 5. PEF₁₃₀ showed the minimum value for the current density (8.533×10^{-7} A/cm²). From the value of the corrosion rate, we know that the corrosion rate of PEF AZ31 was less than that of Bare AZ31 (0.627 mm/year). The corrosion rate was calculated by Tafel analysis using the software. The corrosion rate of PEF₁₃₀ was extremely slow (0.021 mm/year).

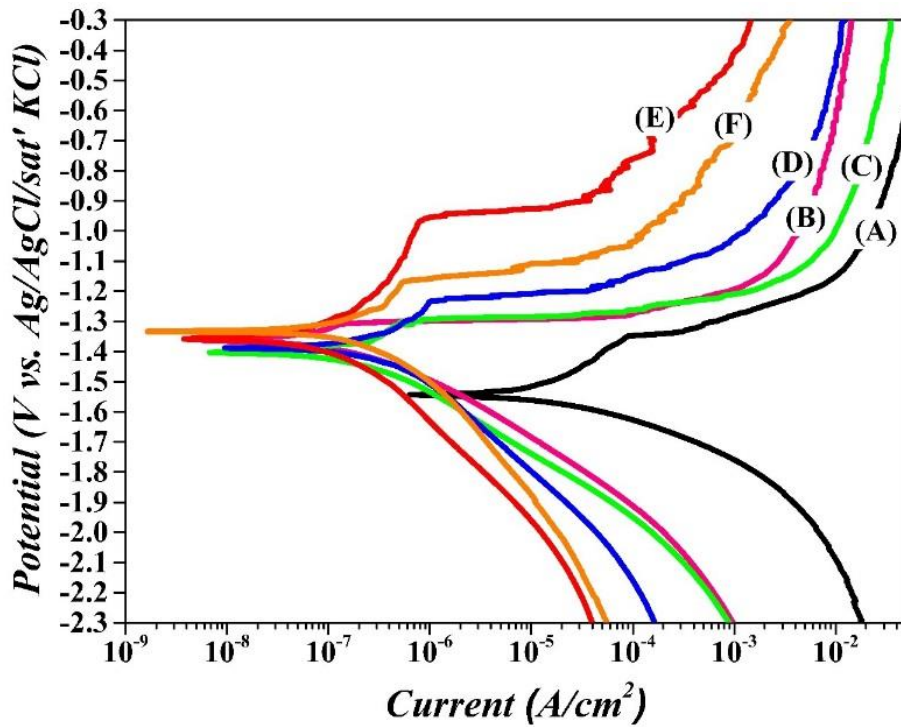


Figure 14. PDP curves of Bare AZ31 (A), PEF₁₀₀ (B), PEF₁₁₀ (C), PEF₁₂₀ (D), PEF₁₃₀ (E), and PEF₁₄₀ (F).

Table 5. Results of the potentiodynamic polarization test for Bare and PEF-coated AZ31. The corrosion potential (E_{corr}), current density (i_{corr}), and corrosion rate (CR) were measured using software (VersaStudio 2.44.4)

Code	E_{corr} (V; I = 0)	i_{corr} (A/cm ²)	CR (mm/year)
Bare	-1.543	2.470×10^{-5}	0.627
PEF ₁₀₀	-1.363	6.811×10^{-6}	0.173
PEF ₁₁₀	-1.403	6.498×10^{-6}	0.165
PEF ₁₂₀	-1.388	3.975×10^{-6}	0.101
PEF ₁₃₀	-1.358	8.533×10^{-7}	0.021
PEF ₁₄₀	-1.334	4.360×10^{-6}	0.111

Figure 15 shows the weight variation for Bare and PEF AZ31 in SBF for one and four weeks. The percent of weight loss after one week of immersion was in the following order: Bare 1.242 (%) > PEF₁₀₀ (0.541 %) > PEF₁₁₀ (0.351 %) > PEF₁₄₀ (0.239%) > PEF₁₂₀ (0.172 %) > PEF₁₃₀ (0.072 %), and the percentage weight loss after four weeks of immersion was in the following order: Bare (5.046%) > PEF₁₀₀ (2.673 %) > PEF₁₁₀ (1.907 %) > PEF₁₂₀ (1.342 %) > PEF₁₄₀ (1.233 %) > PEF₁₃₀ (0.213 %). Thus, PEF₁₃₀ displayed the lowest value for weight loss after one and four weeks of immersion.

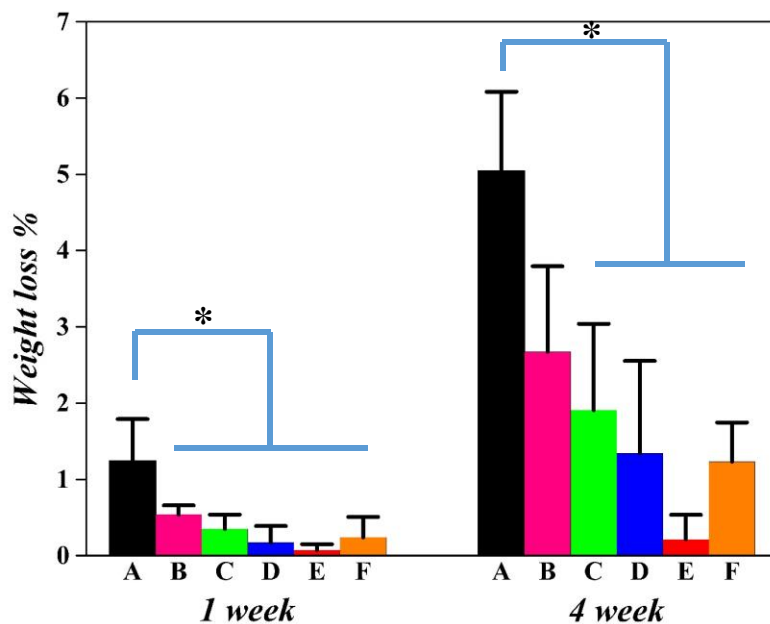


Figure 15. Percentage of weight loss after immersion in SBF for one and four weeks for Bare AZ31 (A), PEF₁₀₀ (B), PEF₁₁₀ (C), PEF₁₂₀ (D), PEF₁₃₀ (E) and PEF₁₄₀ (F). (N = 10) ($p = 0.05$)

3. Tensile test through corrosion

Figure 16 shows the tensile strength–strain curves with optical images of Bare and PEF-coated AZ31 for four weeks (Figure 16A), eight weeks (Figure 16B), and 12 weeks (Figure 16C) of corrosion in SBF. The result shows that the tensile strength of both groups' samples decreased as the duration of immersion in SBF increased. Significantly, the tensile strength of the PEF groups was lower than for the Bare groups. Such results offer visual clues. It was obvious that the PEF-coated AZ31 was subject to more severe localized corrosion than Bare AZ31. We speculate that this localized corrosion was the main reason why the strength loss of the PEF-coated group was faster than that of the Bare group.

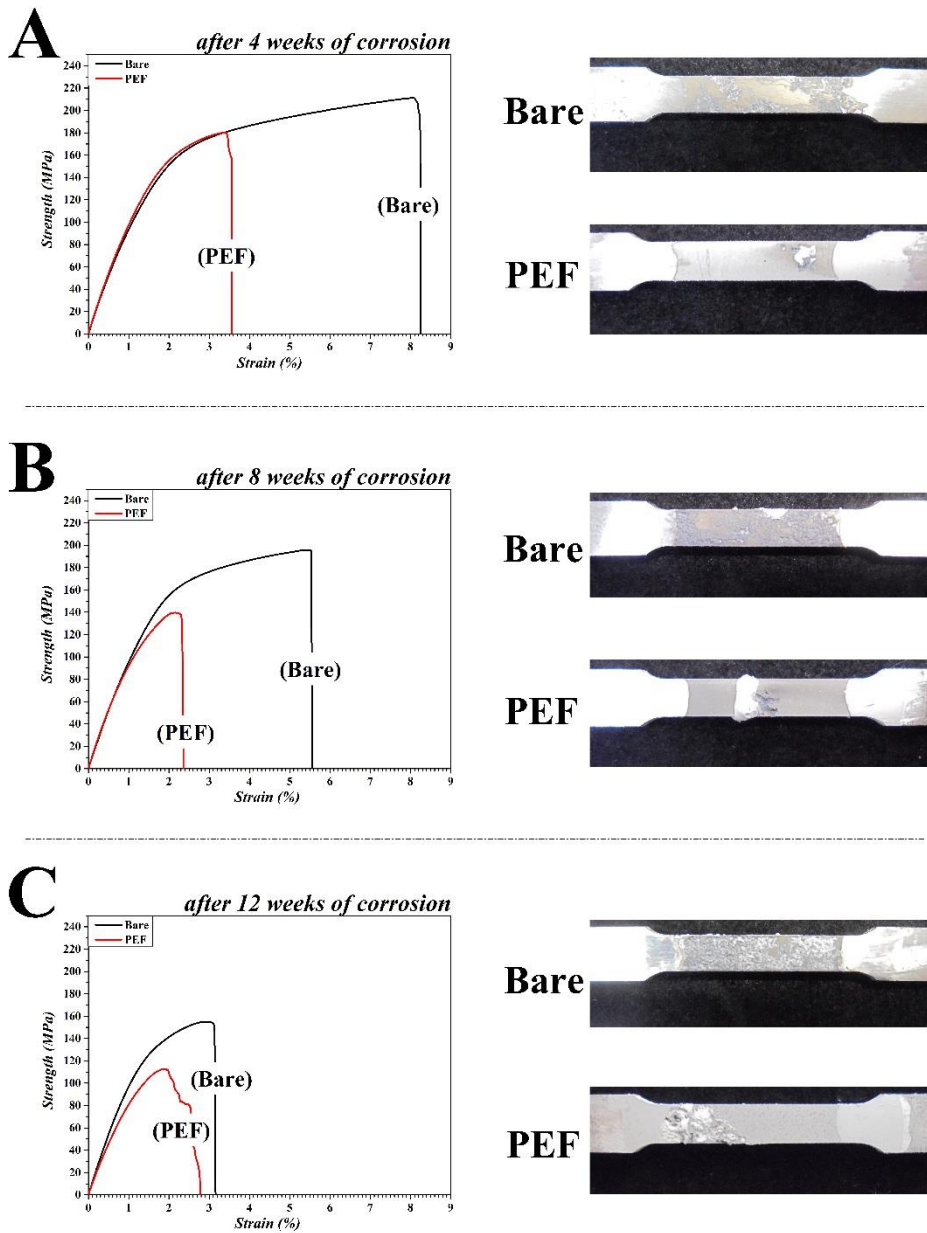


Figure 16. Strength–strain curves with optical images of Bare and PEF-coated AZ31 for: 4 (A), 8 (B), and 12 (C) weeks of corrosion.

Figure 17 shows the mean maximum tensile strength tendency of the Bare and PEF-coated AZ31 after 4, 8, and 12 weeks of corrosion. The tensile strength of both groups decreased as the corrosion time increased; the value of the tensile strength loss in the PEF-coated group was greater than that of the Bare group for any period of time.

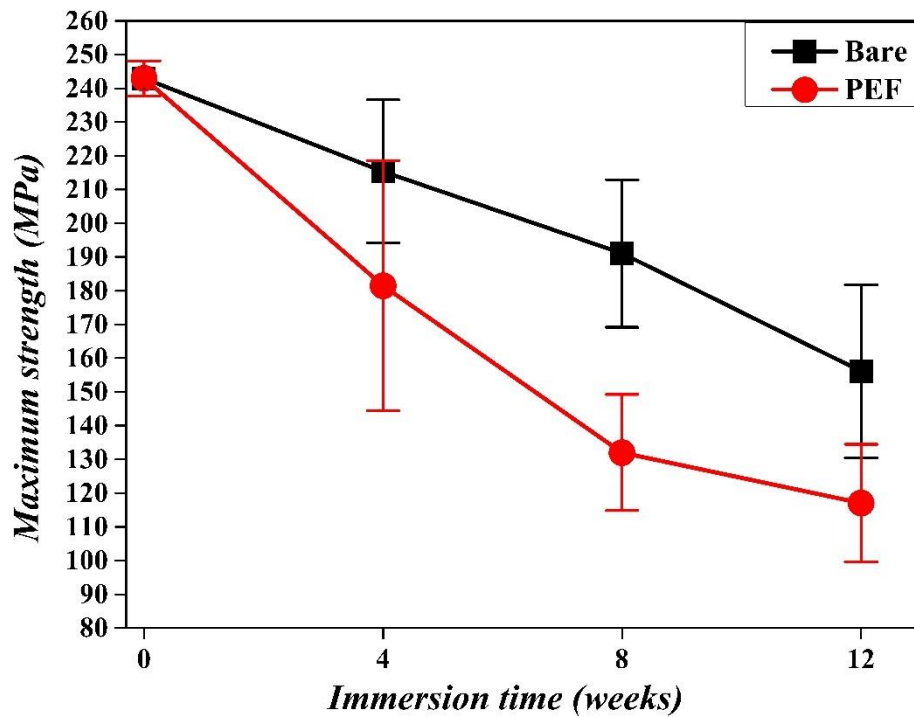


Figure 17. Maximum tensile strength for 4, 8, and 12 weeks of corrosion for Bare and PEF-coated AZ31. (N = 10) ($p = 0.05$)

4. Pitting corrosion analysis

Figure 18 shows the potentiodynamic polarization curves of Bare, PEF-coated, indented Bare (in-Bare), and indented PEF-coated (in-PEF) AZ31. The results clearly show that the curve of the indented PEF-coated AZ31 was obviously moved to the right based on the curve of the PEF-coated AZ31. This means that the current density of the indented PEF-coated AZ31 was increased and that the corrosion behavior increased gradually. However, there was no obvious difference between the Bare and indented Bare AZ31, which means that the indents on the surface of the Bare AZ31 were irrelevant to the corrosion rate.

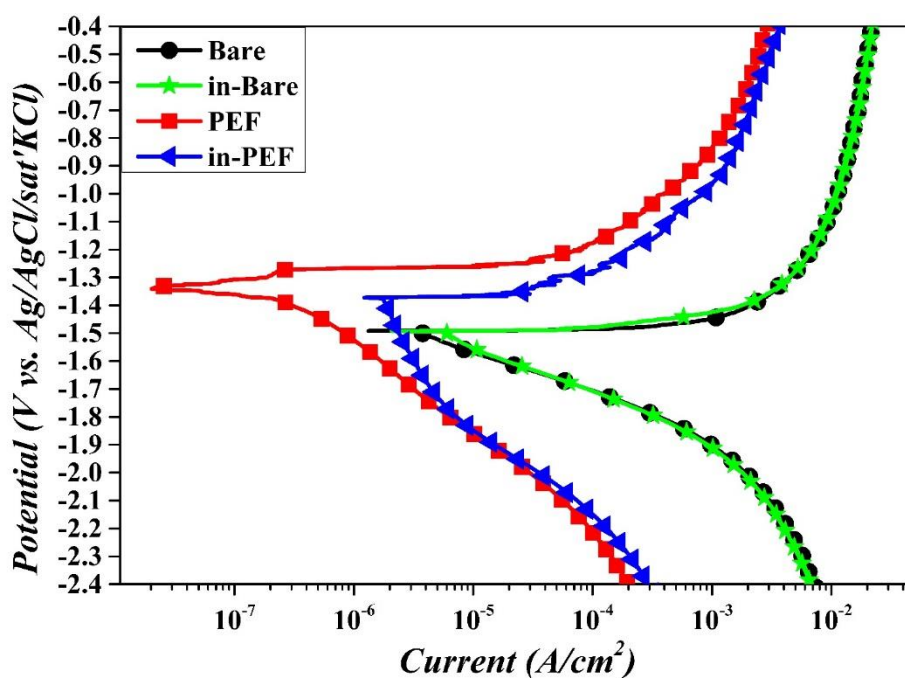


Figure 18. Potentiodynamic polarization curves of Bare, PEF-coated, indented Bare (in-Bare), and indented PEF-coated (in-PEF) AZ31.

Figure 19 shows the optical surface image of the indented Bare and indented PEF-coated AZ31 and after one week of corrosion. According to the images, the corrosion behavior was generated at the indents of indented PEF-coated AZ31, but other areas saw no corrosion. In contrast, the surface of the indented Bare AZ31 seemed to have corroded uniformly. This also means that the indents on the surface of Bare AZ31 were irrelevant to the corrosion behavior.

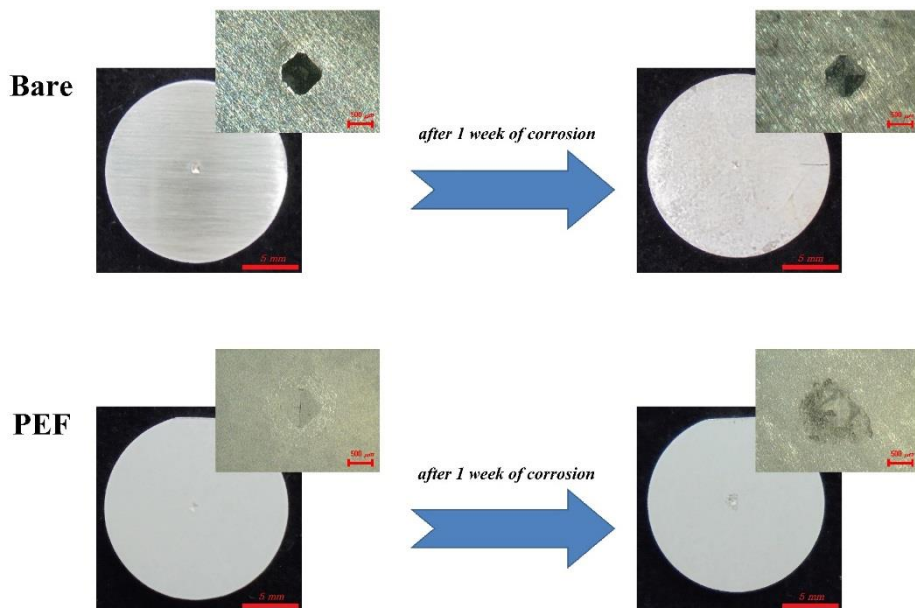


Figure 19. Optical microscopic images of indented Bare and indented PEF-coated AZ31 before and after immersion in SBF for one week.

Figure 20 shows tensile specimens of Bare, PEF-coated, indented Bare (in-Bare), and indented PEF-coated (in-PEF) AZ31 before and after two weeks of corrosion. There is obvious corrosion behavior that was only generated at the indents on the surface of the indented PEF-coated AZ31. The PEF-coated AZ31 seemed not to have corroded and the indented Bare AZ31 was not affected by localized corrosion at the point of indentation.

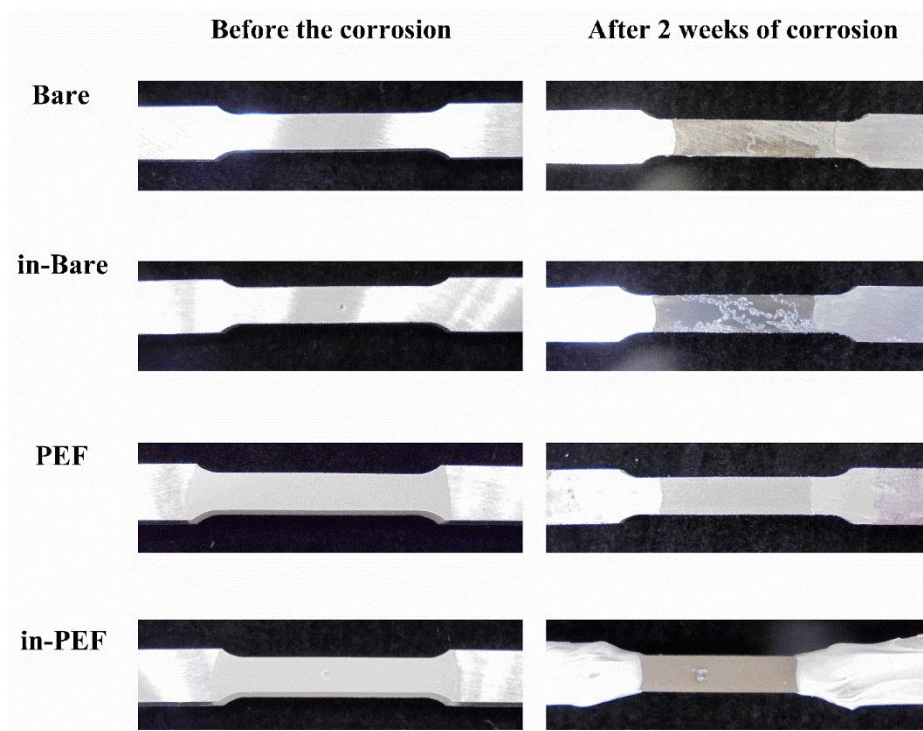


Figure 20. Optical images of Bare, PEF-coated, indented Bare (in-Bare), and indented PEF-coated (in-PEF) AZ31 before and after immersion in SBF for two weeks.

Figure 21 shows the strength–strain curves and mean of maximum strength of the tensile test after two weeks of corrosion for Bare, PEF-coated, indented Bare (in-Bare), and indented PEF-coated (in-PEF) AZ31. We determined how the indents (pitting corrosion) affected the mechanical strength through corrosion by carrying out tensile tests. The result (Figure 21B) showed that there was no difference in the tensile strength between the Bare AZ31 with or without indents. However, when indents were generated on the surface of PEF-coated AZ31 and samples were immersed in SBF for two weeks, the strength was decreased compared to non-indented PEF-coated AZ31.

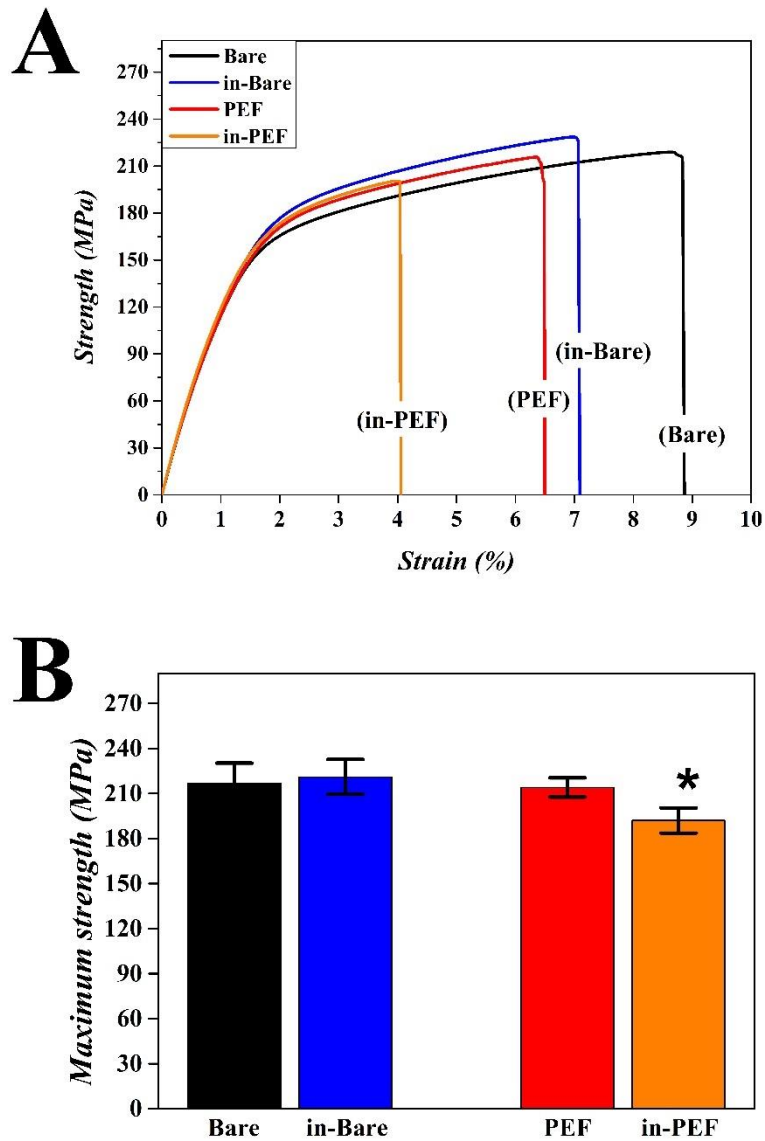


Figure 21. Strength–strain curves (A) and mean maximum strength (B) for two weeks of corrosion of Bare, PEF-coated, indented Bare (in-Bare), and indented PEF-coated (in-PEF) AZ31. (N = 10) ($p = 0.05$)

5. Tensile test through the corrosion of CGD samples

Figure 22 shows the tensile strength–strain curves with optical images of Bare and PEF-coated AZ31 and CGD samples for four weeks (Figure 22A), eight weeks (Figure 22B) and 12 weeks (Figure 22C) of corrosion in SBF. The result shows that the tensile strength of Bare and PEF-coated AZ31 decreased as the duration of immersion increased in SBF. It was obvious that the “corrosion area” of Bare and PEF-coated AZ31 were corroded as shown in the optical images. However, the tensile strength of the CGD sample seemed unchanged and its “corrosion area” seemed not to have demerged or corroded.

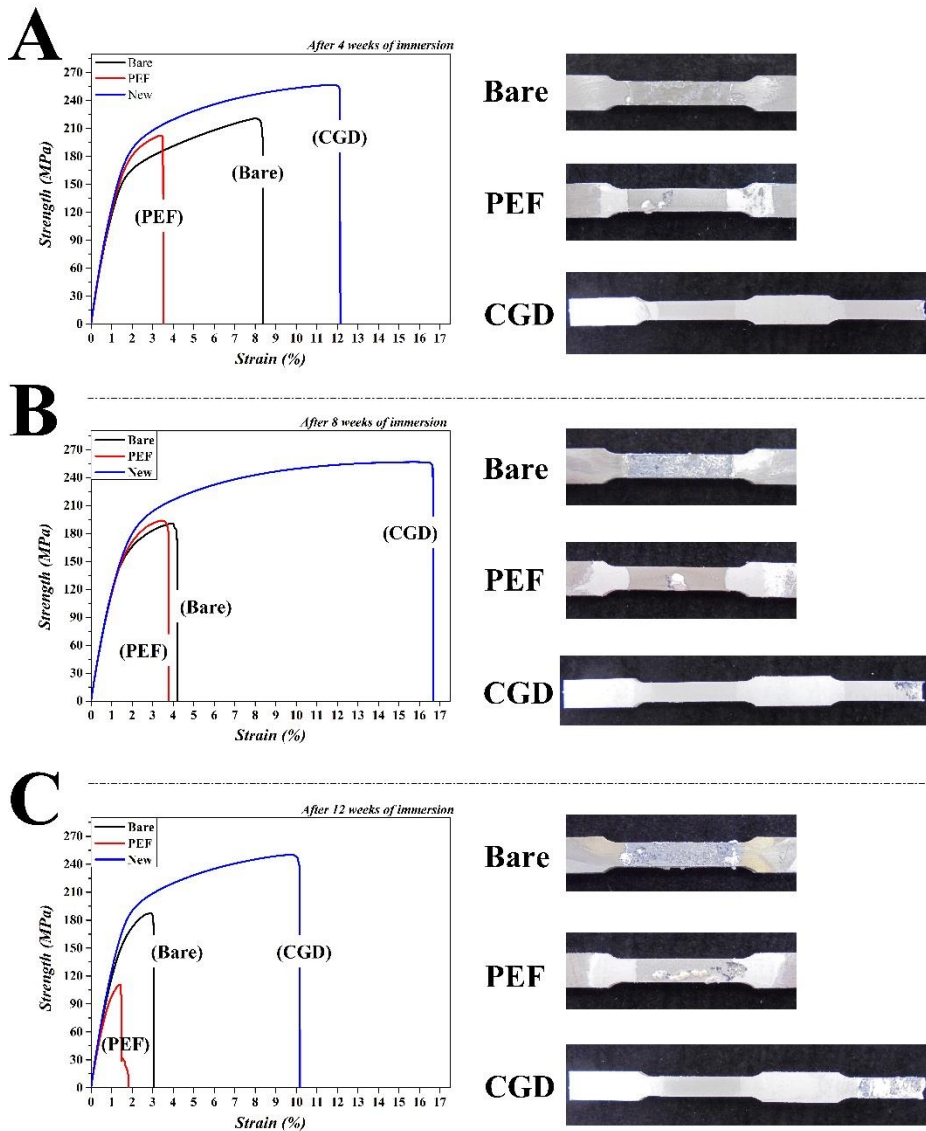


Figure 22. Strength–strain curves with its optical images of Bare and PEF-coated AZ31 and a CGD sample after 4 (A), 8 (B), and 12 (C) weeks of corrosion. (N = 10) ($p = 0.05$)

Figure 23 shows the mean of the maximum tensile strength tendency of the Bare and PEF-coated AZ31 and CGD samples after 4, 8, and 12 weeks of corrosion. The tensile strength of the Bare and PEF-coated groups decreased as the corrosion time increased. In this instance, the value of tensile strength loss in the PEF-coated group was greater than that of the Bare group over any period of time, but the tensile strength of the CGD sample was not decreased over the 12 weeks of corrosion.

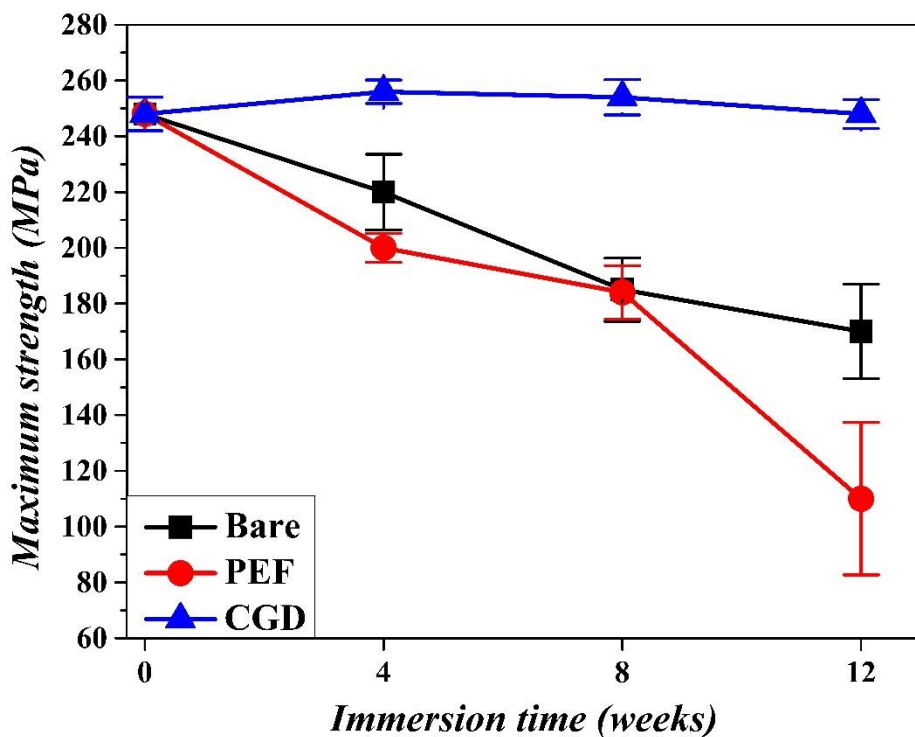


Figure 23. The mean maximum tensile strength for each specified period of corrosion for Bare and PEF-coated AZ31 and the CGD sample. (N = 10) ($p = 0.05$)

IV. DISCUSSION

Anodization is a significant surface treatment technique that utilizes the voltage, current, and frequency (Gu et al., 2012a; Han et al., 2013). Most anodizing treatments for Mg generate an oxide layer (Han et al., 2013). Significantly, anodization allows for the adjustment of film thickness, creates a uniform layer with a porous structure, and involves a short processing time. However, the oxide layer created by anodization has two drawbacks: 1) the formed MgO layer is insufficiently dense and has some cracks (Gu et al., 2012b). 2) It can easily become converted into soluble MgCl_2 in body fluid (Gu et al., 2012a). Both cases lead to an Mg substrate with corrosive damage. Thus, the oxide coating on Mg does not meet the standards demanded of biodegradable implants.

One conventional method of fluoride treatment is the creation of a fluoride coating on the surface of Mg. This method both effectively improves corrosion resistance and has a foolproof processing procedure (Chiu et al., 2007; Yan et al., 2010). It has been mentioned that a fluoride coating is more capable of protecting an Mg substrate than an oxide coating. When Mg samples were immersed in hydrofluoric acid, MgF_2 layers could be created on the Mg surface via chemical conversion, where the dissolution of Mg and the deposition of MgF_2 should occur in a dynamic balance. MgF_2 is insoluble, thus a barrier layer should be established on the Mg surface. Previous studies have reported that the fluoride coating had an excellent protective effect on the Mg substrate and there was no toxicity and biocompatibility *in vitro* (Song and Atrens, 2003) and *in vivo* (Thomann et al., 2010). This means that, to some extent, the fluoride treatment of Mg implants creates a good potential biodegradable implant material due to its utilizable stability and biocompatibility in

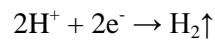
medical applications. However, the processing time for conventional fluoride treatments on Mg should be longer than 24 hours; also, it was difficult to adjust the coating thickness when using this method (Chiu et al., 2007; Thomann et al., 2010; Yan et al., 2010).

Therefore, to create a stable MgF_2 layer on an Mg substrate in an extremely short time, we chose the method of anodization treatment in a fluoride electrolyte.

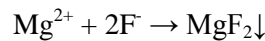
When AZ31 was anodized in molten NH_4HF_2 , many corrosive batteries could be generated on the surface of the alloy. In the anode region, Mg could be dissolved as follows:



The reaction in the negative region was as follows:



The Mg^{2+} reacted with F^- as follows:



When the Mg was applied in the electrolyte at a high voltage, the surface discharged many electric sparks by opening the discharging pores, thus generating a porous structure (Figure 10). The MgF_2 generated on the Mg surface was an insoluble and stable coating and gradually grew until the coating was sufficiently thick to terminate the reaction. All coating formation reactions were completed within 30 seconds (Table 4).

The corrosion behaviors of Bare and PEF-coated AZ31 were investigated. However, the results of polarization with weight loss tests showed a significant difference in the corrosion behaviors of Bare and PEF-coated AZ31.

From these results, the Bare AZ31 exhibited general corrosion behavior in SBF, but the corrosion was hindered after anodization. The polarization test was the most commonly used method of corrosion analysis for detecting metal corrosion potential (E_{corr}) and the corrosion current density (i_{corr}) in SBF. The i_{corr} has a close relationship with the corrosion rate, and its value is inversely proportional to the corrosion resistance (Song and Atrens, 2003), while the value of E_{corr} is directly proportional to the trend in the corrosion resistance (Zhang et al., 2005).

From Table 5, the anodized samples show a lower value for i_{corr} than the Bare AZ31, which means that the corrosion resistance is improved by anodization. From Figure 13, the PEF₁₃₀ shows that the value of the current growth is slow until the breakdown potential of -0.95 V. In addition, we observe that the value of the current at the potential of -0.95 V is larger than the value of the current at the potential of -0.95 V for PEF₁₃₀ because breakdown had already been experienced at a lower potential except for PEF₁₃₀. The breakdown means that the PEF coating is being destroyed by electrochemical deterioration. Once the coating breaks down, the current value is expected to increase (Hornberger et al., 2012), which also means that the corrosion rate will increase.

Depending on the surface (Figure 9) and sectional (Figure 10) images, we can be obviously see that the generated structure pore size and thickness of the PEF coating increases as the anodizing voltage increases. In this study, the coatings of PEF₁₃₀ and PEF₁₄₀ had the same thickness, which may mean that the pore size affected their ability to protect the Mg substrate. When the anodization process was applied at above 130 V, it may produce excessive discharge on the surface of Mg, leading to the generated MgF₂ deposits being damaged by the puncture voltage (Jiang et al., 2014).

In a previous study, the Mg surface was reportedly destroyed by applying a higher voltage than the critical anodization voltage (Jiang et al., 2014). Relating the coating thickness to the results of the corrosion test allows us to summarize that the corrosion resistance increases in accordance with the coating thickness. This phenomenon is in agreement with other literature on fluoride coating (Yan et al., 2010). We conclude that increasing the thickness of the fluoride coating improves the corrosion resistance of Mg.

In addition, H₂ gas release is a problem with Mg implants; however, this problem is considered in the way that the human body endogenously produces gas that can slowly be discharged from the body via sweat glands and body fluids (Kraus et al., 2012). Frischerauer et al. reported that in Mg implants given to rats by μ -CT, the gas released from Mg implants was slowly dissipated over time *in vivo* (Fischerauer et al., 2013). Therefore, improving the corrosion resistance of Mg implants can slow the gas release rate, so the deleterious influence of the gas can be neglected.

Mg and its alloys are subject to various types of corrosive behavior in physiological environments, particularly when local corrosion is involved, which is often the dominant mechanism in the degradation of Mg and Mg alloys (Witte et al., 2008).

A PEF coating could increase the corrosion resistance of AZ31; it is usually considered that a surface coating can improve the corrosion resistance of Mg and maintain its mechanical strength. Unexpectedly, although a PEF coating increased the corrosion resistance of Mg, there was a serious lack of maintenance capacity in the mechanical strength.

As we observed in this work, the PEF coating had a micro porous structure (Figure 10). Perhaps due to the fact that the micro pores caused the thinnest parts of the coating structure to break down in the SBF, the Mg

substrate was revealed in this part and began corroding severely. Therefore, we considered that it might be caused by pitting corrosion on the surface of the PEF-coated AZ31. Pitting corrosion, which penetrates from the surface into the substrate, affects the mechanical behavior of Mg to a much greater extent than uniform corrosion, even for similar degradation rates (Frankel, 1998). One result of pitting corrosion is that it is difficult to maintain the mechanical integrity of implants over the certain period of time in which it would be necessary for medical implants to bear a specific amount of load in a highly corrosive environment. Even if studies of biodegradable Mg are explored continuously, none has yet reported tensile test after corrosion; only a few studies have tested the other mechanical properties of Mg alloys after corrosion (Dezfuli et al., 2017; Krause et al., 2010; Tan et al., 2014; Wang et al., 2011). Thus, the reasons and mechanisms of the changes in tensile strength of PEF-coated AZ31 after corrosion must be discovered and the coating technique should be improved.

The various forms of corrosion that develop with a magnesium implant in the human body are well known. According to our results (Figure 15), we can see that the strength of PEF-coated AZ31 was reduced rapidly compared to Bare AZ31. However, the weight loss percentage of PEF-coated AZ31 was less than that of Bare AZ31. Therefore, we consider pitting corrosion a key factor in these phenomena, as verified by the PEF-coated AZ31 pitting corrosion test.

Although the PEF coating on AZ31 could increase the corrosion resistance, the loss of mechanical strength was too rapid because pitting corrosion was generated on the PEF coating surface. Therefore, we could utilize different surface potentials within Bare and PEF-coated Mg to design a new concept Mg implant, the principle of which is similar to the “sacrificial anode” or “cathodic protection” to expose the Mg substrate at

the end of the PEF-coated Mg. Because the exposed area could easily corrode, the other areas of PEF-coated Mg were protected (Figure 23). Thus, it can be clearly seen from the results (Figures 21 and 22) that the tensile strength of the CGD sample was not decreased during the 12 weeks of corrosion. Perhaps such a discovery and CGD could supplement the PEF coating defects, and could be used in all Mg coatings.

V. CONCLUSION

In this study, our conclusion regarding the surface treatment of AZ31 by plasma electrolytic fluorination is as follows.

1. Uniform and porous structural coatings are formed on PEF-coated AZ31 using applied voltages above 120 V, the diameter of the pore size ranges 600–900 nm, and the coating thickness ranges 1–14 μm . The PEF-coating time is within 30 s.
2. EDS mapping detected that fluoride and magnesium were the main components of the PEF coating.
3. XRD analysis showed that the crystal structure of the PEF coating was MgF_2 .
4. The potentiodynamic polarization test showed that the corrosion rate of the PEF-coated AZ31 was lower than that of the Bare AZ31. Among them, the PEF_{130} showed the lowest corrosion rate.
5. The weight loss test showed that the percentage of weight loss for PEF-coated AZ31 was obviously lower than the Bare AZ31 for one and four weeks immersion. Therein, the PEF_{130} also showed the lowest value ($N = 10$) ($p = 0.05$).
6. The test of tensile strength through corrosion showed that a loss of strength in PEF-coated AZ31 was observably faster than in the Bare AZ31 for 4, 8, and 12 weeks of corrosion ($N = 10$) ($p = 0.05$).
7. The new design (CGD) of the unprecedented Mg implant, can be fully protected the strength of the AZ31 for 4, 8, and 12 weeks of corrosion compared to the Bare and normal PEF coatings ($N = 10$) ($p = 0.05$).

Although, Mg could have increased corrosion resistance after surface treatment, pitting corrosion might rapidly reduce the mechanical strength of the Mg implant, resulting in serious consequences for patients. Perhaps CGD can remedy the disadvantages of applying surface coating technology on biomedical Mg implants.

VI. REFERENCES

Birbilis N, Easton MA, Sudholz A, Zhu S, Gibson M (2009). On the corrosion of binary magnesium-rare earth alloys. *Corrosion Science* 51(3): 683-689.

Cai J, Cao F, Chang L, Zheng J, Zhang J, Cao C (2011). The preparation and corrosion behaviors of MAO coating on AZ91D with rare earth conversion precursor film. *Applied Surface Science* 257(8): 3804-3811.

Chiu KY, Wong MH, Cheng FT, Man HC (2007). Characterization and corrosion studies of fluoride conversion coating on degradable Mg implants. *Surface and Coatings Technology* 202(3): 590-598.

Dezfuli SN, Leeftang S, Huan Z, Chang J, Zhou J (2017). Fabrication of novel magnesium-matrix composites and their mechanical properties prior to and during in vitro degradation. *Journal of the Mechanical Behavior of Biomedical Materials* 67: 74-86.

Eliezer A, Witte F (2010). Corrosion behavior of magnesium alloys in biomedical environments. *Advanced Materials Research*. Trans Tech Publ. pp 17-20.

Ezhilselvi V, Nithin J, Balaraju JN, Subramanian S (2016). The influence of current density on the morphology and corrosion properties of MAO coatings on AZ31B magnesium alloy. *Surface and Coatings Technology* 288: 221-229.

Fischerauer SF, Kraus T, Wu X, Tangl S, Sorantin E, Hänzli AC, *et al.* (2013). In vivo degradation performance of micro-arc-oxidized magnesium implants: A micro-CT study in rats. *Acta Biomaterialia* 9(2): 5411-5420.

Flitt HJ, Schweinsberg DP (2005). Evaluation of corrosion rate from polarisation curves not exhibiting a Tafel region. *Corrosion Science* 47(12): 3034-3052.

Frankel G (1998). Pitting corrosion of metals a review of the critical factors. *Journal of the Electrochemical Society* 145(6): 2186-2198.

Ganeshan S, Shang S, Wang Y, Liu Z-K (2009). Effect of alloying elements on the elastic properties of Mg from first-principles calculations. *Acta Materialia* 57(13): 3876-3884.

Gu Y, Bandopadhyay S, Chen C-f, Guo Y, Ning C (2012a). Effect of oxidation time on the corrosion behavior of micro-arc oxidation produced AZ31 magnesium alloys in simulated body fluid. *Journal of Alloys and Compounds* 543: 109-117.

Gu Y, Chen C-f, Bandopadhyay S, Ning C, Zhang Y, Guo Y (2012b). Corrosion mechanism and model of pulsed DC microarc oxidation treated AZ31 alloy in simulated body fluid. *Applied Surface Science* 258(16): 6116-6126.

Han XG, Zhu F, Zhu XP, Lei MK, Xu JJ (2013). Electrochemical corrosion behavior of modified MAO film on magnesium alloy AZ31 irradiated by high-intensity pulsed ion beam. *Surface and Coatings Technology* 228, Supplement 1: S164-S170.

Hornberger H, Virtanen S, Boccaccini AR (2012). Biomedical coatings on magnesium alloys – A review. *Acta Biomaterialia* 8(7): 2442-2455.

Hort N, Huang Y, Fechner D, Störmer M, Blawert C, Witte F, *et al.* (2010). Magnesium alloys as implant materials—principles of property design for Mg–RE alloys. *Acta biomaterialia* 6(5): 1714-1725.

Iglesias C, Bodelón O, Montoya R, Clemente C, Garcia-Alonso M, Rubio J, *et al.* (2015). Fracture bone healing and biodegradation of AZ31 implant in rats. *Biomedical Materials* 10(2): 025008.

Jiang HB, Kim YK, Ji JH, Park IS, Bae TS, Lee MH (2014). Surface modification of anodized Mg in ammonium hydrogen fluoride by various voltages. *Surface and Coatings Technology* 259, Part B: 310-317.

Kannan MB, Raman RS (2008). Evaluating the stress corrosion cracking susceptibility of Mg–Al–Zn alloy in modified-simulated body fluid for orthopaedic implant application. *Scripta Materialia* 59(2): 175-178.

Kirkland NT, Birbilis N, Walker J, Woodfield T, Dias GJ, Staiger MP (2010). In - vitro dissolution of magnesium–calcium binary alloys: Clarifying the unique role of calcium additions in bioresorbable magnesium implant alloys. *Journal of Biomedical Materials Research Part B: Applied Biomaterials* 95(1): 91-100.

Kirkland N, Birbilis N, Staiger M (2012). Assessing the corrosion of biodegradable magnesium implants: a critical review of current methodologies and their limitations. *Acta biomaterialia* 8(3): 925-936.

Kraus T, Fischerauer SF, Hänzli AC, Uggowitzer PJ, Löffler JF, Weinberg AM (2012). Magnesium alloys for temporary implants in osteosynthesis: In vivo studies of their degradation and interaction with bone. *Acta Biomaterialia* 8(3): 1230-1238.

Krause A, Von der Höh N, Bormann D, Krause C, Bach F-W, Windhagen H, *et al.* (2010). Degradation behaviour and mechanical properties of magnesium implants in rabbit tibiae. *Journal of materials science* 45(3): 624.

Kunzler TP, Drobek T, Schuler M, Spencer ND (2007). Systematic study of osteoblast and fibroblast response to roughness by means of surface-morphology gradients. *Biomaterials* 28(13): 2175-2182.

Li J, Zheng Z, Li S, Ren W, Zhang Z (2006). Preparation and galvanic anodizing of a Mg–Li alloy. *Materials Science and Engineering: A* **433**(1): 233-240.

Lin D-J, Hung F-Y, Jakfar S, Yeh M-L (2016). Tailored coating chemistry and interfacial properties for construction of bioactive ceramic coatings on magnesium biomaterial. *Materials & Design* 89: 235-244.

Liu C, Wang Y, Zeng R, Zhang X, Huang W, Chu P (2010). In vitro corrosion degradation behaviour of Mg–Ca alloy in the presence of albumin. *Corrosion Science* 52(10): 3341-3347.

Müller WD, Nascimento ML, Zeddies M, Córscico M, Gassa LM, Fernández Lorenzo de Mele MA (2007). Magnesium and its alloys as degradable biomaterials. *Materials Research* 10.

Mousa HM, Hussein KH, Pant HR, Woo HM, Park CH, Kim CS (2016). In vitro degradation behavior and cytocompatibility of a bioceramic anodization films on the biodegradable magnesium alloy. *Colloids and Surfaces A: Physicochemical and Engineering Aspects* 488: 82-92.

Němcová A, Skeldon P, Thompson GE, Pacal B (2013). Effect of fluoride on plasma electrolytic oxidation of AZ61 magnesium alloy. *Surface and Coatings Technology* 232: 827-838.

Ostrowski NJ, Lee B, Roy A, Ramanathan M, Kumta PN (2013). Biodegradable poly(lactide-co-glycolide) coatings on magnesium alloys for orthopedic applications. *Journal of Materials Science: Materials in Medicine* 24(1): 85-96.

Peixoto Barbosa D, Knörschild G (2009). Anodization of Mg-alloy AZ91 in NaOH solutions. *Surface and Coatings Technology* 203(12): 1629-1636.

Razavi M, Fathi M, Savabi O, Vashae D, Tayebi L (2015). In vivo assessments of bioabsorbable AZ91 magnesium implants coated with nanostructured fluoridated hydroxyapatite by MAO/EPD technique for biomedical applications. *Materials Science and Engineering: C* **48**: 21-27.

Shi P, Ng WF, Wong MH, Cheng FT (2009). Improvement of corrosion resistance of pure magnesium in Hanks' solution by microarc oxidation with sol-gel TiO₂ sealing. *Journal of Alloys and Compounds* 469(1-2): 286-292.

Song G-L, Shi Z (2014). Corrosion mechanism and evaluation of anodized magnesium alloys. *Corrosion Science* 85: 126-140.

Song G, Atrens A (2003). Understanding Magnesium Corrosion—A Framework for Improved Alloy Performance. *Advanced Engineering Materials* 5(12): 837-858.

Song G, Song S (2007). A Possible Biodegradable Magnesium Implant Material. *Advanced Engineering Materials* 9(4): 298-302.

Staiger MP, Pietak AM, Huadmai J, Dias G (2006). Magnesium and its alloys as orthopedic biomaterials: A review. *Biomaterials* 27(9): 1728-1734.

Sun W, Zhang G, Tan L, Yang K, Ai H (2016). The fluoride coated AZ31B magnesium alloy improves corrosion resistance and stimulates bone formation in rabbit model. *Materials Science and Engineering: C* 63: 506-511.

Takadama H, Hashimoto M, Mizuno M, Kokubo T (2004). Round-robin test of SBF for in vitro measurement of apatite-forming ability of synthetic materials. *Phosphorus Research Bulletin* 17: 119-125.

Tan L, Wang Q, Lin X, Wan P, Zhang G, Zhang Q, *et al.* (2014). Loss of mechanical properties in vivo and bone-implant interface strength of AZ31B magnesium alloy screws with Si-containing coating. *Acta biomaterialia* 10(5): 2333-2340.

Thomann M, Krause C, Angrisani N, Bormann D, Hassel T, Windhagen H, *et al.* (2010). Influence of a magnesium-fluoride coating of magnesium-based implants (MgCa0.8) on degradation in a rabbit model. *Journal of Biomedical Materials Research Part A* 93A(4): 1609-1619.

Vojtěch D, Čížová H, Volenec K (2006). Investigation of magnesium-based alloys for biomedical applications. *Kovove Mater* **44**: 211-223.

Wan P, Yuan C, Tan L, Li Q, Yang K (2014). Fabrication and evaluation of bioresorbable PLLA/magnesium and PLLA/magnesium fluoride hybrid composites for orthopedic implants. *Composites Science and Technology* **98**: 36-43.

Wang H, Shi Z (2011a). In vitro biodegradation behavior of magnesium and magnesium alloy. *Journal of Biomedical Materials Research Part B: Applied Biomaterials* **98**(2): 203-209.

Wang J (2006). *Analytical electrochemistry*. edn. John Wiley & Sons.

Wang J, Tang J, Zhang P, Li Y, Wang J, Lai Y, *et al.* (2012). Surface modification of magnesium alloys developed for bioabsorbable orthopedic implants: A general review. *Journal of Biomedical Materials Research Part B: Applied Biomaterials* **100B**(6): 1691-1701.

Wang Q, Tan L, Xu W, Zhang B, Yang K (2011b). Dynamic behaviors of a Ca-P coated AZ31B magnesium alloy during in vitro and in vivo degradations. *Materials Science and Engineering: B* **176**(20): 1718-1726.

Wang Y, Wang F, Xu M, Zhao B, Guo L, Ouyang J (2009). Microstructure and corrosion behavior of coated AZ91 alloy by microarc oxidation for biomedical application. *Applied Surface Science* **255**(22): 9124-9131.

Wilke BM, Zhang L, Li W, Ning C, Chen C-f, Gu Y (2016). Corrosion performance of MAO coatings on AZ31 Mg alloy in simulated body fluid vs. Earle's Balance Salt Solution. *Applied Surface Science* **363**: 328-337.

Willbold E, Kaya A, Kaya R, Beckmann F, Witte F (2011). Corrosion of magnesium alloy AZ31 screws is dependent on the implantation site. *Materials Science and Engineering: B* **176**(20): 1835-1840.

Witte F (2015). Reprint of: The history of biodegradable magnesium implants: A review. *Acta Biomaterialia* **23**, Supplement: S28-S40.

Witte F, Fischer J, Nellesen J, Vogt C, Vogt J, Donath T, *et al.* (2010). In vivo corrosion and corrosion protection of magnesium alloy LAE442. *Acta Biomaterialia* **6**(5): 1792-1799.

Witte F, Hort N, Vogt C, Cohen S, Kainer KU, Willumeit R, *et al.* (2008). Degradable biomaterials based on magnesium corrosion. *Current Opinion in Solid State and Materials Science* 12(5–6): 63-72.

Xu L, Yamamoto A (2012). Characteristics and cytocompatibility of biodegradable polymer film on magnesium by spin coating. *Colloids and Surfaces B: Biointerfaces* 93: 67-74.

Xu L, Yu G, Zhang E, Pan F, Yang K (2007). In vivo corrosion behavior of Mg - Mn - Zn alloy for bone implant application. *Journal of Biomedical Materials Research Part A* 83(3): 703-711.

Yan T, Tan L, Xiong D, Liu X, Zhang B, Yang K (2010). Fluoride treatment and in vitro corrosion behavior of an AZ31B magnesium alloy. *Materials Science and Engineering: C* 30(5): 740-748.

Zeng R-c, Zhang J, Huang W-j, Dietzel W, Kainer KU, Blawert C, *et al.* (2006). Review of studies on corrosion of magnesium alloys. *Transactions of Nonferrous Metals Society of China* 16: s763-s771.

Zhang F, Cai S, Xu G, Shen S, Li Y, Zhang M, *et al.* (2016a). Corrosion behavior of mesoporous bioglass-ceramic coated magnesium alloy under applied forces. *Journal of the Mechanical Behavior of Biomedical Materials* 56: 146-155.

Zhang S, Zhang X, Zhao C, Li J, Song Y, Xie C, *et al.* (2010). Research on an Mg–Zn alloy as a degradable biomaterial. *Acta biomaterialia* 6(2): 626-640.

Zhang Y, Tang S, Hu J, Lin T (2016b). Formation mechanism and corrosion resistance of the hydrophobic coating on anodized magnesium. *Corrosion Science* 111: 334-343.

Zhang Y, Yan C, Wang F, Li W (2005). Electrochemical behavior of anodized Mg alloy AZ91D in chloride containing aqueous solution. *Corrosion Science* 47(11): 2816-2831.

ABSTRACT (IN KOREAN)

플라즈마 전해 불화처리와 희생양극 디자인이 생흡수성 마그네슘합금의 내구성 강화에 미치는 영향

<지도교수: 김 광 만 >

연세대학교 대학원 치의학과

강 형 과

생분해성 금속재료인 마그네슘(Mg) 및 그 합금은 정형외과, 심혈관 내과 및 치과 분야에서 많은 연구를 부단히 진행하고 있다. 하지만, 마그네슘 임플란트는 생리적 환경에서의 내부식성이 낮음으로 인해 의학적 용도에 적용되기엔 아직 한계가 있다.

본 연구에서는 Mg합금의 일종인 AZ31을 사용 하였다. AZ31의 내 부식성을 향상시키기 위해 고농도의 불화물 전해질을 사용하여 PEF 코팅처리(플라즈마 전해 불화처리)를 시행하였다. 그리고 PEF코팅된 AZ31의 표면형태, 코팅 두께 및 코팅 성분을 관찰하였고 전기화학 부식시험 및 무게감소시험을 진행하여 부식특성을 평가하였다. PEF 코팅된 AZ31과 코팅되지 않은 AZ31을 인공체액속에 4, 8, 12주 동안 침지한 후 인장강도를 측정하여 비교하였다. 대부분 표면처리된 마그네슘은 주로 공식현상이 생기기 때문에 이를 관찰하기 위하여 경도기로 샘플표면에 압흔을 내어 공식시험을 진행 및 분석하였다. 그

리고 AZ31의 급속한 부식이 발생하는 것을 방지하기 위하여 희생양극 원리를 이용한 부식유도형 디자인(CGD)을 개발하여 비교 분석하였다.

결과에서는 PEF코팅표면은 다공성 구조였고 기공크기는 600-900 nm, 코팅두께는 1-14 μm 이다. PEF코팅의 주요성분은 불화마그네슘이다. 전기화학부식시험 및 무게감소시험에서 PEF코팅된 AZ31은 인공체액속에서 코팅되지 않은 AZ31과 비교하였을 때 내부식성이 효과적으로 개선되었다. 부식한뒤 인장강도시험에서 PEF코팅된 AZ31의 인장강도는 코팅하지 않은 AZ31보다 낮았다. 공식시험을 통하여 PEF코팅된 AZ31의 강도가 급속히 저하되는 결과를 초래하는 주요 원인은 공식이라는 것을 입증하였다. 따라서 부식유도형 디자인은 AZ31의 강도를 일정한 침적시일내에서도 완벽하에 보호할 수 있었다.

PEF코팅은 생물학적으로 유리한 구조이면서 AZ31의 내식성을 높일 수 있지만 PEF코팅된 AZ31은 생흡수 과정에서 공식이 생성되어 기계적 파절을 일으킬 수 있기 때문에 임상적으로 사용되기에는 아직 한계가 있다. 부식유도형 디자인은 PEF코팅기술의 단점을 해결했을 뿐만 아니라 이는 생흡수성 마그네슘임플란트의 임상적 적용에 중요한 역할이 될 것이다.

핵심되는 말: 마그네슘 임플란트, 플라즈마 전해 불화처리, 인장강도, 내부식성, 생분해성, 공식, 부식유도형 디자인